Check for updates

JGR Oceans

RESEARCH ARTICLE
10.1029/2025JC023673

# Circumpolar Effects of a Velocity-Restoring Scheme for Antarctic Fast Ice on Shelf Waters and Ice Shelf Melt Simulated by NEMO4-SI$^3$

**N. Pirlet[1], T. Fichefet[1], M. Vancoppenolle[2], C. de Lavergne[2], and N. C. Jourdain[3]**

[1]Earth and Life Institute-Climate (ELI-C), Université Catholique de Louvain (UCLouvain), Louvain-la-Neuve, Belgium, [2]Sorbonne Université, CNRS, IRD, MNHN, Laboratoire d'Océanographie et du Climat, LOCEAN/IPSL, Paris, France, [3]Institut des Geosciences de l'Environnement, Université Grenoble Alpes/CNRS/IRD/G-INP/INRAE, Grenoble, France

**Key Points:**

- Beneath fast ice, the simulated upper-ocean stratification is enhanced, further isolating cold surface waters from warmer subsurface waters
- Where fast ice occurs, shallow mixed layers let warm water intrude into ice shelf cavities, raising basal melt by 15.8%
- Improved coastal polynya representation increases sea ice production and dense shelf water formation in key Antarctic source regions

**Supporting Information:**

Supporting Information may be found in the online version of this article.

**Correspondence to:**

M. Vancoppenolle,
martin.vancoppenolle@locean.ipsl.fr

**Citation:**

Pirlet, N., Fichefet, T., Vancoppenolle, M., de Lavergne, C., & Jourdain, N. C. (2026). Circumpolar effects of a velocity-restoring scheme for Antarctic fast ice on shelf waters and ice shelf melt simulated by NEMO4-SI$^3$. *Journal of Geophysical Research: Oceans*, *131*, e2025JC023673. https://doi.org/10.1029/2025JC023673

Received 29 OCT 2025
Accepted 9 SEP 2026

**Author Contributions:**

**Conceptualization:** N. Pirlet, T. Fichefet, M. Vancoppenolle
**Formal analysis:** N. Pirlet, C. de Lavergne
**Funding acquisition:** T. Fichefet
**Investigation:** N. Pirlet
**Methodology:** N. Pirlet
**Project administration:** T. Fichefet, M. Vancoppenolle
**Resources:** C. de Lavergne
**Software:** N. Pirlet
**Supervision:** T. Fichefet, M. Vancoppenolle

© 2026 The Author(s). Journal of Geophysical Research: Oceans published by Wiley Periodicals LLC on behalf of American Geophysical Union.
This is an open access article under the terms of the Creative Commons Attribution License, which permits use, distribution and reproduction in any medium, provided the original work is properly cited.

**Abstract** Dense water formation in the Southern Ocean plays a key role in the global ocean overturning circulation, affecting the distribution of heat, carbon, oxygen, and nutrients. Fast ice stays immobile while blocking sea ice flow, favoring the opening of coastal polynyas, where intense air-sea exchanges drive sea ice production and ocean densification. Antarctic fast ice representation is notoriously poor in Earth system models, and is thus considered a potential cause of model biases in dense water formation. Here we assess the impact of a sea ice velocity-restoring representation of Antarctic fast ice on Antarctic shelf water properties and ice shelf melt using NEMO4-SI$^3$ simulations with and without velocity-restoring. By improving the location and shape of coastal polynyas, fast ice redistributes sea ice production and promotes Dense Shelf Water formation in several key source regions. In contrast, beneath extensive fast ice tongues, the reduced brine rejection associated with lower sea ice production limits mixed layer deepening, leading to fresher surface waters, which are then advected into downstream polynyas. The enhanced upper-ocean stratification beneath fast ice isolates warm subsurface waters from the surface and favors their intrusion into nearby ice shelf cavities, increasing ice shelf basal melt. As a result, ice shelf basal melt increases overall by 15.8% in the simulation including fast ice. These results support that ESMs studies with an Antarctic focus would gain from a physically-based representation of Antarctic fast ice.

**Plain Language Summary** The Southern Ocean around Antarctica is key to the global climate system. In this region, dense water forms on the continental shelf and sinks to the deep ocean, carrying heat, carbon, oxygen, and nutrients around the globe. The ocean also melts Antarctic ice shelves—large, floating extensions of the Antarctic ice sheet. Earth system models (ESMs) try to represent these processes but often do so inaccurately. One important issue is that most models neglect fast ice, immobile sea ice attached to the coast, grounded icebergs, and the Antarctic ice shelf calving fronts. Fast ice strongly influences nearby areas of open-water, called coastal polynyas, which are important sites for sea ice growth and the formation of dense water. In this study, we add a representation of fast ice in an ocean-sea ice model and examine how it affects Antarctic shelf waters. We find that adding fast ice makes shelf waters denser in some areas, but fresher beneath and downstream of long stretches of fast ice. Overall, representing fast ice increases the ice shelf melt rate. Our results show that ESMs would gain in realism on the Antarctic continental shelf with a proper representation of fast ice.

## 1. Introduction

Dense waters originating from the ocean surface at high latitudes make up the vast majority of the World Ocean's volume (Gordon et al., 2001). Once formed through heat loss and/or salt gain, these waters sink to depth and spread across the globe, carrying chemical elements into the abyss, hence information about atmosphere-ice-ocean interactions. The primary sources of these dense waters are the high-latitude North Atlantic Ocean and the coastal Antarctic regions. The densest global-scale water mass, named Antarctic Bottom Water (AABW), mainly originates from Antarctic shelves (Orsi et al., 1999). The formation, circulation and decay of AABW influence global climate dynamics via heat and carbon uptake and transport (Marinov et al., 2008; Patara & Böning, 2014; Purkey & Johnson, 2010). In particular, the lifecycle of AABW is considered as a key process shaping the World Ocean's influence on climate variability on centennial-to-millennial timescales (Brook & Buizert, 2018; Sarmiento & Toggweiler, 1984; Sigman et al., 2010).

**Validation:** N. Pirlet
**Visualization:** N. Pirlet
**Writing – original draft:** N. Pirlet
**Writing – review & editing:** T. Fichefet, M. Vancoppenolle, C. de Lavergne, N. C. Jourdain

Dense Shelf Water (DSW) forms on the Antarctic continental shelf at four main sites: in the Weddell Sea (Gill, 1973), in the Ross Sea (Jacobs et al., 1970), off East Antarctica near Adélie Land (Rintoul & Bullister, 1999), and near Cape Darnley (Ohshima et al., 2013), with tight links to the cryosphere (Gordon et al., 2001). The main driver is coastal polynyas (Any non-linear shaped opening enclosed between drift ice and the coast or between drift ice and an ice front. Polynyas may contain brash ice and/or be covered with new ice, nilas or young ice; World Meteorological Organization, 2014) where intense sea ice production enhances the surface water salinity and density through brine rejection (Morales Maqueda et al., 2004; Tamura et al., 2008; Williams et al., 2016), forming High-Salinity Shelf Water (HSSW). Additionally, water mass transformations occurring in ocean cavities beneath floating ice shelves generate supercooled water called Ice Shelf Water (ISW) and, more generally, release freshwater from basal melt, which contributes to modifying DSW properties (Meredith & Brandon, 2017). Ultimately, a portion of DSW flows off the shelf and cascades down the continental slope while mixing with Circumpolar Deep Water (CDW) and fresher Antarctic Surface Water (AASW) (Akhoudas et al., 2021; Orsi et al., 1999) to form AABW (Silvano et al., 2023).

Fast ice is the stationary component of the sea ice cover which forms and remains fast along the coast, where it is attached to the shore, to an ice wall, to an ice front, between shoals or grounded icebergs (Fraser et al., 2023; World Meteorological Organization, 2014). Around Antarctica, fast ice typically forms a narrow coastal band extending from a few kilometers to several tens of kilometers offshore, although widths exceeding 100–200 km are reported in some regions (Fraser et al., 2023). Most Antarctic fast ice is seasonal, forming during austral autumn, persisting through winter, and breaking up or melting during spring and summer, while some regions support multiyear fast ice that can survive several melt seasons (Fraser et al., 2021). The Antarctic fast ice cover reaches a maximum extent, 601,000 $km^2$ on average, in October and a minimum extent of 221,000 $km^2$ in March (Fraser et al., 2021). Although it contributes only 4%–13% of the total Antarctic sea ice extent, fast ice exerts a strong influence on coastal Antarctic oceanography by modulating air-sea exchanges, coastal polynya activity, shelf water transformation, and DSW formation, thereby affecting the production of AABW and the properties of the global overturning circulation (Fraser et al., 2023).

AABW, as simulated by large-scale ocean-sea ice models used in climate studies, suffers from major biases, still poorly understood (Behrens et al., 2016; Heuzé, 2021). Many Earth system models (ESM) generate dense water in the Southern Ocean, but often at incorrect locations (mostly in the central Weddell and Ross Seas) and for the wrong reasons (Heuzé, 2021; Heuzé et al., 2013). This model weakness likely arises from three sources: (a) resolution-related limitations, including the inadequate representation of downslope currents and deep convection in open ocean regions, (b) lack of ice shelf cavities in models, and (c) missing or poorly represented physical processes, such as the formation of coastal polynyas and fast ice. The present study focuses only on the third. Indeed, key drivers of coastal polynyas are not well considered, such as fast ice, tidal currents or katabatic winds (Lemieux et al., 2018; Mathiot et al., 2010). This has detrimental implications on the Southern Ocean's circulation, surface heat and carbon fluxes, and biogeochemical cycles, undermining confidence in global climate projections (Intergovernmental Panel on Climate Change, 2022).

A strong connection between fast ice and coastal polynyas has been highlighted in both hemispheres (Fraser et al., 2012; Mahoney et al., 2007; Massom et al., 1998; Nihashi & Ohshima, 2015). In the Arctic, the understanding that fast ice is primarily controlled by bathymetry and the thickness of pressure ridges (Gorbunov et al., 2008; Mahoney et al., 2014) has led to significant modeling progress (Dupont et al., 2022; Lemieux et al., 2015, 2016). Adding a bottom friction term to the sea ice momentum equation and tensile strength to the viscous-plastic rheology usually used in sea ice models enables successful simulation of Arctic fast ice and improved ocean dynamics (e.g., Liu et al., 2025; Sterlin et al., 2024). However, such a fast ice formulation is not suitable for the Southern Ocean, where the continental shelf is deeper and interactions with thick tabular icebergs grounded on the continental shelf play a dominant role (Fraser et al., 2012; Massom et al., 1998; Olivé Abelló et al., 2025; Vancoppenolle et al., 2025).

This context highlights the need for improved Antarctic fast ice representation in ocean-sea ice models. Early efforts to address this issue include those of Kusahara et al. (2010), who prescribed grounded icebergs in an ocean-sea ice model (Hasumi, 2006) to block sea ice advection in three coastal polynya areas: Cape Darnley, Mertz Glacier, and Ninnis Glacier. Cougnon et al. (2013) used the fast ice climatology from Fraser et al. (2012) to reproduce the two main areas of permanent fast ice near the Mertz Glacier Tongue in the Regional Ocean Modeling System (Shchepetkin & McWilliams, 2005). Similar methods to Kusahara et al. (2010) were also used



21699291, 2026, 10, Downloaded from https://agupubs.onlinelibrary.wiley.com/doi/10.1029/2025JC023673 by Universite Catholique De Louvain, Wiley Online Library on [06/10/2026]. See the Terms and Conditions (https://onlinelibrary.wiley.com/terms-and-conditions) on Wiley Online Library for rules of use; OA articles are governed by the applicable Creative Commons License

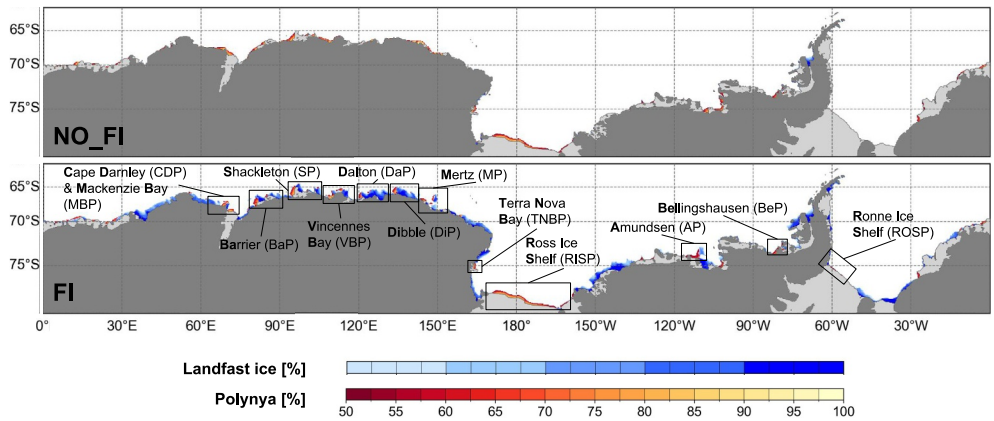



**Figure 1.** March-to-October coastal polynya (red shading) and fast ice (blue shading) frequency of occurrence averaged over 2013–2017 in the simulations without (NO_FI; upper panel) and with (FI; lower panel) the velocity-restoring fast ice scheme (see Pirlet et al., 2025). Frequencies represent the fraction of time during March–October for which a grid cell is classified as fast ice or coastal polynya. The location of the 13 major Antarctic coastal polynyas are highlighted and labeled using the abbreviations defined in the figure.

to simulate the Amundsen Sea polynya in an ocean-sea ice model (Bett et al., 2020; Nakayama et al., 2014). Kusahara et al. (2017) improved this approach by introducing multiyear fast ice as constant-thickness ice shelf grid cells in the East Antarctic region. More recently, Huot et al. (2021), and Van Achter, Fichefet, Goosse, Pelletier, et al. (2022) demonstrated that incorporating the geographical distribution of large grounded icebergs and accounting for sea ice tensile strength led to a realistic simulation of fast ice in a regional ocean-sea ice model. These refinements improved coastal polynya representation and dense water properties in the Adélie Land and Totten Glacier areas. However, these studies have been limited to small Antarctic regions due to current limitations in observation and modeling of grounded icebergs, leaving the broader impacts of Antarctic fast ice mostly unexplored.

Very recently, using the ocean-sea ice model NEMO-SI$^3$ (Nucleus for European Modeling of the Ocean—Sea Ice modeling Integrated Initiative), we developed a method that empirically but accurately represents Antarctic fast ice on a circumpolar scale by restoring sea ice velocity to zero where and when fast ice is present in the observational data set of Fraser et al. (2020), which is the first pan-Antarctic mapping of fast ice. Figure 1 displays the frequency of occurrence of coastal polynyas and fast ice without (NO_FI) and with (FI) the method. We found that this not only improves the simulation of fast ice, as expected, but also yields coastal polynyas in much better agreement with observations and enhanced sea ice production in coastal polynya regions (Pirlet et al., 2025).

In the present study, we build upon this work and explore the effects of our velocity-restoring fast ice scheme on Antarctic shelf water properties and ice shelf melt simulated by NEMO4-SI$^3$. The model, the fast ice scheme, forcings, experimental design, and observations used for validation purposes are described in Section 2. The results are then analysed and discussed in Section 3. A general discussion and concluding remarks are finally given in Section 4.

## 2. Materials and Methods

The same model, configuration, and experimental design as in Pirlet et al. (2025) are used. In what follows, we cover the aspects essential to this study.

### 2.1. The Ocean-Sea Ice Model NEMO-SI$^3$

We use the NEMO modeling platform (version 4.2.2; Madec et al., 2023). The ocean component of NEMO simulates ocean dynamics using a three-dimensional, free-surface, hydrostatic, and Boussinesq framework for primitive equations, combined with finite-difference discretization methods. The advection of tracers is handled through fourth-order and second-order flux-corrected transport schemes for horizontal and vertical processes, respectively (Zalesak, 2012). The TEOS-10 equation of state is approximated via a polynomial function (Roquet et al., 2015). Adiabatic eddy mixing is represented using the Gent and Mcwilliams (1990) parameterization, while



21699291, 2026, 10, Downloaded from https://agupubs.onlinelibrary.wiley.com/doi/10.1029/2025JC023673 by Universite Catholique De Louvain, Wiley Online Library on [06/10/2026]. See the Terms and Conditions (https://onlinelibrary.wiley.com/terms-and-conditions) on Wiley Online Library for rules of use; OA articles are governed by the applicable Creative Commons License

internal wave mixing follows the scheme proposed by de Lavergne et al. (2020). A free-slip lateral boundary condition is applied to momentum, except at the South Orkney Islands (situated at the northern tip of the Antarctic Peninsula), where a no-slip condition is implemented, following Mathiot and Jourdain (2023). This localized adjustment accounts for the influence of subgrid-scale bathymetric variations on water mass properties. Additional modeling choices, including momentum advection, lateral diffusion of momentum and tracers, vertical mixing, convection, double diffusion, and bottom boundary layer treatment, follow the approach described by Storkey et al. (2018).

For sea ice, we utilize SI$^3$, a dynamic-thermodynamic continuum model (Rousset et al., 2015; Vancoppenolle et al., 2023) which operates directly on the ocean grid. SI$^3$ incorporates energy- and salt-conserving thermodynamics (Vancoppenolle et al., 2009), five ice categories to capture subgrid-scale ice thickness variations (Bitz et al., 2001; Lipscomb, 2001), horizontal ice dynamics, with an adaptive elastic-viscous-plastic (aEVP) formulation for the rheology term (Kimmritz et al., 2016), and a second-order-moment-conserving scheme for horizontal advection (Prather, 1986).

### 2.2. The Velocity-Restoring Fast Ice Scheme

SI$^3$ includes an option to restore sea ice velocity toward zero where and when fast ice is observed (Pirlet et al., 2025). The method combines (a) a daily, satellite-based fast ice mask constructed from the bi-weekly, 1 km data set of Fraser et al. (2020), upscaled to model resolution, (b) a restoring scheme that damps sea ice velocity to near-zero where and when fast is observed, and (c) an adaptation of the code that precludes new ice growth in compact fast ice conditions to avoid unrealistic ice thickness.

The velocity restoring is applied at each sub-time step of the aEVP solver (i.e., 120 sub-iterations per model time step of 1,350 s). The damping is not based on a classical continuous-time relaxation, but instead corresponds to a strong sub-iteration damping within the aEVP solver that rapidly restores sea ice velocities toward zero within the fast ice mask, while avoiding the numerical instabilities associated with imposing a strict zero-velocity boundary condition. The chosen $\tau = 0.01$ value implies that sea ice velocity is divided by $\sim 100$ at every sub-cycle. As a result, velocities are never equal to 0 but are several orders of magnitude smaller than the velocity of drifting pack ice (e.g., $<5 \times 10^{-4}$ m s$^{-1}$). The scheme acts only on existing model sea ice and does not prescribe sea ice where the model simulates open-water. The standard model imposes a minimum amount of open-water (to account for cracks in pack ice), and we suppress that feature in fast ice. This modification avoids boundless ice growth in the fast ice zone and unrealistically thick fast ice that would otherwise result from the SI$^3$ default minimum open-water fraction (5%). By contrast, there is no need to limit the melting of compact fast ice, as melting is mostly purely vertical and not much confined to cracks, as new ice formation is.

### 2.3. The eANT025 Configuration

As our study focuses on water masses over the Antarctic continental shelf, we developed the regional eANT025 configuration, detailed in Pirlet et al. (2025), as an adaptation of the global eORCA025 configuration (Mathiot & Jourdain, 2023). This setup encompasses the Antarctic sea ice zone, the Southern Ocean and Antarctic sub-ice-shelf cavities, with a single open boundary at 30°S. The model operates on a quasi-equal zonal and meridional grid spacing at a nominal resolution of 0.25°, corresponding to less than 12 km at 65°S. While high-resolution simulations (<2 km) have been shown to better resolve processes involved in AABW formation (e.g., Golledge et al., 2025), such configurations remain computationally prohibitive for long-term, fully coupled climate simulations. Current and next-generation ESM (e.g., CMIP7 models) typically employ ocean horizontal resolutions ranging from 1° to 0.25° (approximately 100–10 km; Roberts et al., 2025). In this context, our 0.25° configuration is designed to operate within the resolution class used for climate simulation. The vertical discretization consists of 121 levels, with layer thickness increasing non-linearly from 1 m at the surface to approximately 20 m between 100 and 1,000 m depth, and up to 200 m near the ocean floor. Partial step representation (Barnier et al., 2006) is used for bathymetry and ice shelf draft. The ocean circulation below ice shelves and the ocean-ice thermodynamic exchanges follow Mathiot et al. (2017), with the same options and parameter values as in Mathiot and Jourdain (2023), including the three-equation formulation of Jenkins (1991) for calculating heat and salt budget at the ice-ocean interface.



21699291, 2026, 10, Downloaded from https://agupubs.onlinelibrary.wiley.com/doi/10.1029/2025JC023673 by Universite Catholique De Louvain, Wiley Online Library on [06/10/2026]. See the Terms and Conditions (https://onlinelibrary.wiley.com/terms-and-conditions) on Wiley Online Library for rules of use; OA articles are governed by the applicable Creative Commons License

21699291, 2026, 10, Downloaded from https://agupubs.onlinelibrary.wiley.com/doi/10.1029/2025JC023673 by Universite Catholique De Louvain, Wiley Online Library on [06/10/2026]. See the Terms and Conditions (https://onlinelibrary.wiley.com/terms-and-conditions) on Wiley Online Library for rules of use; OA articles are governed by the applicable Creative Commons License

At the bottom, the ocean component is forced by geothermal heat fluxes mapped by Goutorbe et al. (2011). At the surface, atmospheric conditions from the fifth-generation of the European Center for Medium-Range Weather Forecasts atmospheric reanalysis (ERA5, Hersbach et al., 2020) are prescribed through the Coupled Ocean-Atmosphere Response Experiment bulk formulae (Griffies et al., 2009; Large & Yeager, 2004). This includes three-hourly wind, air temperature, and humidity, all at 10 m height, as well as surface radiation fluxes (shortwave and longwave), precipitation (both solid and liquid), and sea level pressure. A snowfall correction has been applied to prevent boundless thickening of fast ice in narrow bays (see Pirlet et al., 2025). At the ocean surface, a sea surface freshwater flux correction is applied. This flux is diagnosed from a dedicated simulation in which a restoring term toward observed sea surface salinities (World Ocean Atlas 2018 [WOA2018]; Zweng et al., 2019) is interactive and saved at monthly frequency over the period 2001–2017. The diagnosed restoring values are then used to construct a climatological freshwater correction that is prescribe as a forcing in the main simulations. This approach is crucial to keep the main simulations as realistic as possible whilst avoiding the restoring term from altering the model response to the activation of the fast ice scheme (e.g., Swart et al., 2023). Furthermore, the freshwater flux correction is set to zero in the first 150 km from the Antarctic coast to avoid interference with coastal polynyas and fast ice (Pirlet et al., 2025). At the model northern boundary (30°S), a flow relaxation scheme (Engedahl, 1995) is applied to three-dimensional ocean variables, while a Flather scheme (Flather, 1994) is used for barotropic velocities and sea surface elevation. Boundary conditions are derived from Ocean Reanalysis System 5 data (Zuo et al., 2019), interpolated onto the 121 model levels. No tides are prescribed at the boundary.

The default SI$^3$ configuration provided in the NEMO distribution (Rousset et al., 2015; Vancoppenolle et al., 2023) is used with some modifications. The configuration includes five subgrid-scale ice thickness categories and two vertical ice layers. Ice-ocean and ice-atmosphere stresses are computed using drag coefficients of $5.0 \times 10^{-3}$ and $1.4 \times 10^{-3}$, respectively. The ice strength thickness parameter P* is set to $1.5 \times 10^4$ N m$^{-1}$. Snow thermal conductivity is fixed at 0.35 W m$^{-1}$ K$^{-1}$, and a minimum open-water fraction of 5% is enforced, consistent with Boucher et al. (2020) and Mathiot and Jourdain (2023).

### 2.4. Experimental Design

We conducted a series of simulations to assess the influence of the velocity-restoring fast ice scheme on the Antarctic shelf water properties and ice shelf melt. Throughout this study, terms such as representing, including, or incorporating fast ice refer specifically to the implementation of this velocity-restoring fast ice scheme. They do not imply a fully prognostic representation of fast ice within the sea ice model.

To establish initial ocean and sea ice conditions, we performed a spin-up simulation covering the period 1979–2001. This spin-up was initialized from rest, using ocean temperatures and salinities from the WOA2018 climatology (Locarnini et al., 2018; Zweng et al., 2019), along with sea ice concentration and thickness fields from a 1980–2004 global simulation (G06; Storkey et al., 2018). The velocity-restoring fast ice scheme was not activated in the spin-up. Then we conducted two simulations, FI (Fast Ice) and NO_FI (No Fast Ice), which respectively activate and deactivate the fast ice scheme. These experiments span the complete years of fast ice observations, from 2001 to 2017 (Fraser et al., 2020). In both simulations, restoring toward observed sea surface salinities is not interactive but instead forced with a climatological surface freshwater flux (see Section 2.3) at monthly timescale. The drift in simulated hydrography from 1979 to 2017 is small on the continental shelves (Figure S14 in Supporting Information S1).

Since we focus on the impact of a surface feature (fast ice) on continental shelf water properties and ice shelf melt, sufficient simulation time is required for these effects to fully develop. To ensure that the effects of fast ice reach the bottom shelf waters, we analyze only the five final years of each simulation (2013–2017). Sensitivity tests using longer averaging windows show that the magnitude of the response varies slightly, but the sign and spatial structure of the FI-NO_FI differences remain unchanged (see Figure S1 in Supporting Information S1), indicating that our conclusions are robust to the choice of the 5-year mean period. The only large change is found for the mixed layer depth (MLD) in the Weddell Sea, likely reflecting strong regional internal variability. Using the final 5 years therefore represents a compromise between a sufficiently long period and late enough from initial conditions.

21699291, 2026, 10, Downloaded from https://agupubs.onlinelibrary.wiley.com/doi/10.1029/2025JC023673 by Universite Catholique De Louvain, Wiley Online Library on [06/10/2026]. See the Terms and Conditions (https://onlinelibrary.wiley.com/terms-and-conditions) on Wiley Online Library for rules of use; OA articles are governed by the applicable Creative Commons License

### 2.5. Observational Products Used for Model Evaluation

Several observation-based products were used to evaluate simulated sea ice production, ocean temperature and salinity on the continental shelf, and MLD. All products were linearly interpolated onto the ∼10 km model grid for comparison with model fields.

First, we compare the model sea ice production in polynyas to the Nakata et al. (2021) data set. This data set is based on AMSR-E passive microwave satellite records to delineate coastal polynyas according to retrieved frazil and thin ice, and combined with ERA5 atmospheric reanalyses to calculate sea ice production. Sea ice production is diagnosed daily on a polar stereographic grid with a spatial resolution of 6.25 km.

To assess the model ocean temperatures and salinities over the continental shelf, we use the Southern Ocean temperature and salinity profile compilation of Zhou et al. (2025). This data set compiles conservative temperature and absolute salinity profiles computed from ship Conductivity Temperature Depth (CTD), Argo floats and seal-borne profilers in the Southern Ocean (90°S–45°S) since 1972.

The observational climatology of MLD from Sallée et al. (2021) is used to evaluate the model performance. This data set combines the three same types of oceanographic observations to maximize spatial and temporal coverage. Sallée et al. (2021) adopted a density-based method to determine MLD, defining it as the depth where potential density exceeds the 10 m surface density by 0.03 kg $m^{-3}$.

Among the available circum-Antarctic ice shelf melt rate data sets (e.g., Depoorter et al., 2013; Liu et al., 2015; Paolo et al., 2023), we selected the estimates from Rignot et al. (2013), Adusumilli et al. (2020), and Davison et al. (2023) for comparison with the simulated melt rates. These data sets provide complementary constraints on ice shelf basal melt, combining a mass-budget approach with altimetry-derived thickness change estimates and this from different observational periods. Because the melt rate estimates of Adusumilli et al. (2020) do not extend south of 81.5°S, we excluded the Ross and Filchner-Ronne Ice Shelves estimates for this data set from our comparison.

## 3. Results

### 3.1. Sea Ice Production

Figures 2a–2c show the spatial distribution of the cumulative high (>4 m) sea ice production between March and October averaged over 2003–2010 from the NO_FI simulation, FI simulation, and the satellite-based estimates of Nakata et al. (2021, hereafter referred to as observations), respectively. As discussed in detail in Pirlet et al. (2025), representing fast ice largely improves the location and shape of Antarctic coastal polynyas (Figure 1) and their associated sea ice production. Nevertheless, two notable discrepancies emerge when the model output is compared to observations. First, the model simulates a more widespread distribution of high sea ice production than presented in Nakata et al. (2021), because their data set does not include sea ice production outside the polynya domain. Second, the model overestimates sea ice production in the Weddell Sea near the grounded iceberg A23a due to the influence of local fast ice.

Pirlet et al. (2025) also showed that including fast ice does not increase the total sea ice production, but reshapes its geographical distribution across the continental shelf: sea ice production is enhanced in coastal polynyas and at fast ice margins, while reduced beneath fast ice. However, as shown in Figure 2d, the model underestimates sea ice production within coastal polynyas relative to the estimates of Nakata et al. (2021). Outside coastal polynyas, no comparison is possible because observational estimates are not available.

The difference in sea ice production between the two simulations is shown in Figure 2e, with most variations concentrated shoreward of the 1,500 m isobath, which is used by Portela et al. (2022) to define the continental shelf boundary. Figure S2 in Supporting Information S1, which replicates Figure 2e for the 2003–2010 period, reveals a similar pattern of differences and Figure S3a in Supporting Information S1 shows that nearly all anomalies are statistically significant at the 95% confidence level ($p < 0.05$). Over the continental shelf, the annual total sea ice production averaged over 2013–2017 is 9,019 ± 218 $km^3$ $yr^{-1}$ in FI and 9,089 ± 146 $km^3$ $yr^{-1}$ in NO_FI. The inclusion of fast ice therefore reduces the total sea ice production over the continental shelf by about 70 $km^3$ $yr^{-1}$, corresponding to less than 1% of the total. We further define three regions: the

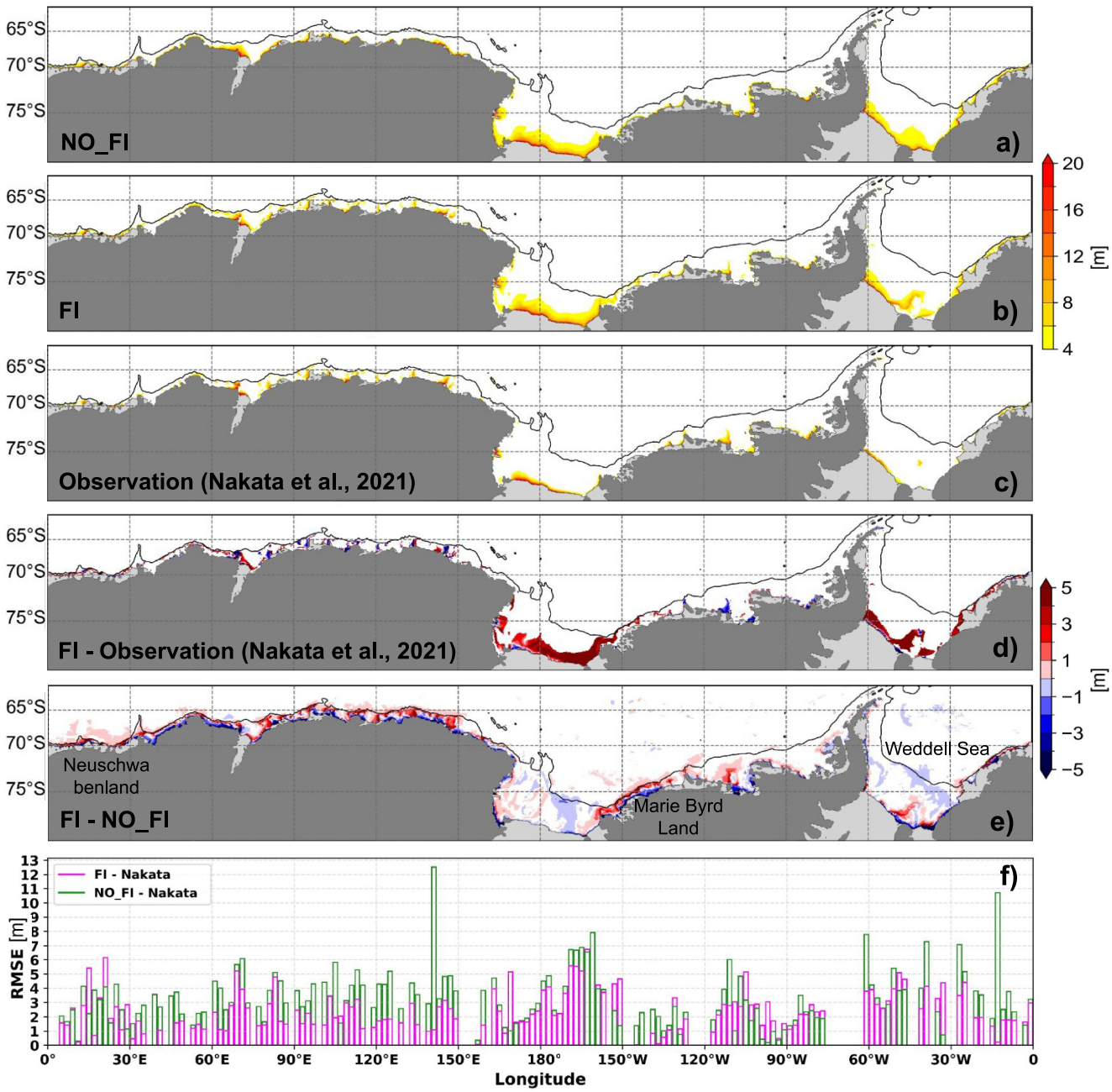



**Figure 2.** Total sea ice production between March and October averaged over 2003–2010 in the NO_FI (a) and FI (b) simulations. (c) Same but from satellite-based estimates of Nakata et al. (2021). Differences of sea ice production between the FI simulation and the satellite-based estimates of Nakata et al. (2021) (2003–2010; d), and between the FI and NO_FI simulations (e) over the period 2013–2017. The black contour indicates the continental shelf border (1,500 m depth). Some important locations mentioned in the text are indicated in panel (e). (f) Root-mean-square error of sea ice production over the continental shelf relative to Nakata et al. (2021) for 2003–2010, averaged in 2° longitude bins. FI-Nakata et al. (2021) is shown in pink and NO_FI-Nakata et al. (2021) in green.

FAST region includes grid cells with >50% fast ice frequency of occurrence, the POLYNYA region consists of cells with >25% polynya frequency of occurrence, and the ELSE region encompasses the remainder of the continental shelf. From NO_FI to FI, the annual sea ice production is redistributed with a decrease of 841 $km^3$ $yr^{-1}$ in the FAST ice region, almost entirely offset by a 330 $km^3$ $yr^{-1}$ increase in the POLYNYA region and a 441 $km^3$ $yr^{-1}$ increase in the ELSE region.



21699291, 2026, 10, Downloaded from https://agupubs.onlinelibrary.wiley.com/doi/10.1029/2025JC023673 by Universite Catholique De Louvain, Wiley Online Library on [06/10/2026]. See the Terms and Conditions (https://onlinelibrary.wiley.com/terms-and-conditions) on Wiley Online Library for rules of use; OA articles are governed by the applicable Creative Commons License

21699291, 2026, 10, Downloaded from https://agupubs.onlinelibrary.wiley.com/doi/10.1029/2025JC023673 by Universite Catholique De Louvain, Wiley Online Library on [06/10/2026]. See the Terms and Conditions (https://onlinelibrary.wiley.com/terms-and-conditions) on Wiley Online Library for rules of use; OA articles are governed by the applicable Creative Commons License

Together, Figures 2d and 2e confirm that, while the fast ice representation alone is insufficient for the model to fully reproduce the observed sea ice production, it plays a crucial role in reducing the gap between the model and observations in coastal polynyas (Figure 2f). This reduction in sea ice production bias is also found when the production off the 1,500 m isobath is included (see Figure S4 in Supporting Information S1), indicating that the improvement is not due to an offshore displacement of the sea ice production region. Consequently, improvements in the representation of Antarctic shelf water properties can be expected, at least locally. However, some areas, such as off the coast of Marie Byrd Land (around 150°W) and off the coast of Neuschwabenland (between 0°E and 30°E), exhibit increased biases. Additional model improvements, such as a more realistic representation of katabatic winds, tidal currents, and leads, may be necessary to further reduce the sea ice production gap with observations.

### 3.2. Water Mass Properties at the Continental Shelf Scale

Before analysing the changes of the continental shelf water properties, we evaluate the model output in comparison to the conservative temperature and absolute salinity measurements compiled by Zhou et al. (2025) at the continental shelf scale. For consistency, only data located over the continental shelf and covering 2013–2017 were selected. Only the model grid cells corresponding to the locations of observations were retained, ensuring the closest comparison between data sets. The number of observational data available per grid cell (summed vertically and over time) is shown in the maps of Figure 3. While some regions are well sampled, others are entirely devoid of data (see Figure S5 in Supporting Information S1 for the longitudinal distribution), a limitation taken into account in the validation of the continental shelf water mass properties.

For the ice growth period (March to October; Figures 3a and 3c) and the summer period (November to February; Figures 3e and 3g), both simulations accurately reproduce the observed average vertical salinity profile. Similarly, the simulated average vertical temperature profile also aligns with observations, although the vertical gradient is weaker than observed. This comparison gives us confidence in the model ability to reproduce the average shelf water characteristics. On average, across these sparsely observed regions, the representation of fast ice has little impact on the model performance.

We then examined the differences between the two simulations in more detail by analyzing anomalies using not only grid cells where observations are available, but also all the other continental shelf model data. The anomaly profiles for salinity and temperature exhibit a similar shape across the two seasons. For salinity (Figures 3b and 3f), a surface freshening of approximately $-0.06$ g kg$^{-1}$ is observed in FI compared to NO_FI, along with a positive anomaly below 250 m. For temperature (Figures 3d and 3h), FI exhibits a weak surface cooling ($<-0.01$°C) and a warming between 150 and 600 m ($>0.02$°C) relative to NO_FI. The weak amplitude of the averaged anomalies indicates that the circumpolar-scale impact of Antarctic fast ice on the large-scale mean vertical T-S structure is modest. This is consistent with the absence of net changes in total sea ice production over the continental shelf (only a redistribution), as discussed in the previous section. Therefore, a spatial analysis is called for to better understand the localized impacts of the fast ice representation on the shelf water properties.

### 3.3. MLD

We now turn to the winter MLD, which we use as an indicator of the convective mixing associated with sea ice production. Figures 4a–4c show the MLD simulated in NO_FI, FI and derived from Sallée et al. (2021), all using the same MLD definition (De Boyer Montégut et al., 2004). The NO_FI and FI simulations capture the observed MLD pattern at the continental shelf scale. However, Figure 4d reveals substantial differences between the FI simulation and Sallée et al. (2021), particularly over the continental shelf. While this could reflect model limitations, observational uncertainty remains large—many parts of the Southern Ocean are poorly sampled (cf. Figure 3), requiring spatial and temporal interpolation (Sallée et al., 2021), which affects the accuracy of the MLD estimates. Nevertheless, the comparison remains instructive: it suggests that the model simulates MLD shallower than observed off the continental shelf margin and deeper than observed over the shelf (Figure 4d). In well-known sites of DSW formation, such as the western Ross and Weddell Sea shelves, the model predicts much deeper MLD than the observational product, but this is where MLD is most sensitive to small hydrographic differences, and could also reflect limits in the observational sampling.

Figure 4e illustrates the MLD response to the activation of the velocity-restoring fast ice scheme. MLD decreases beneath fast ice, indicating weaker mixing there in the FI simulation. In contrast, MLD increases at the fast ice

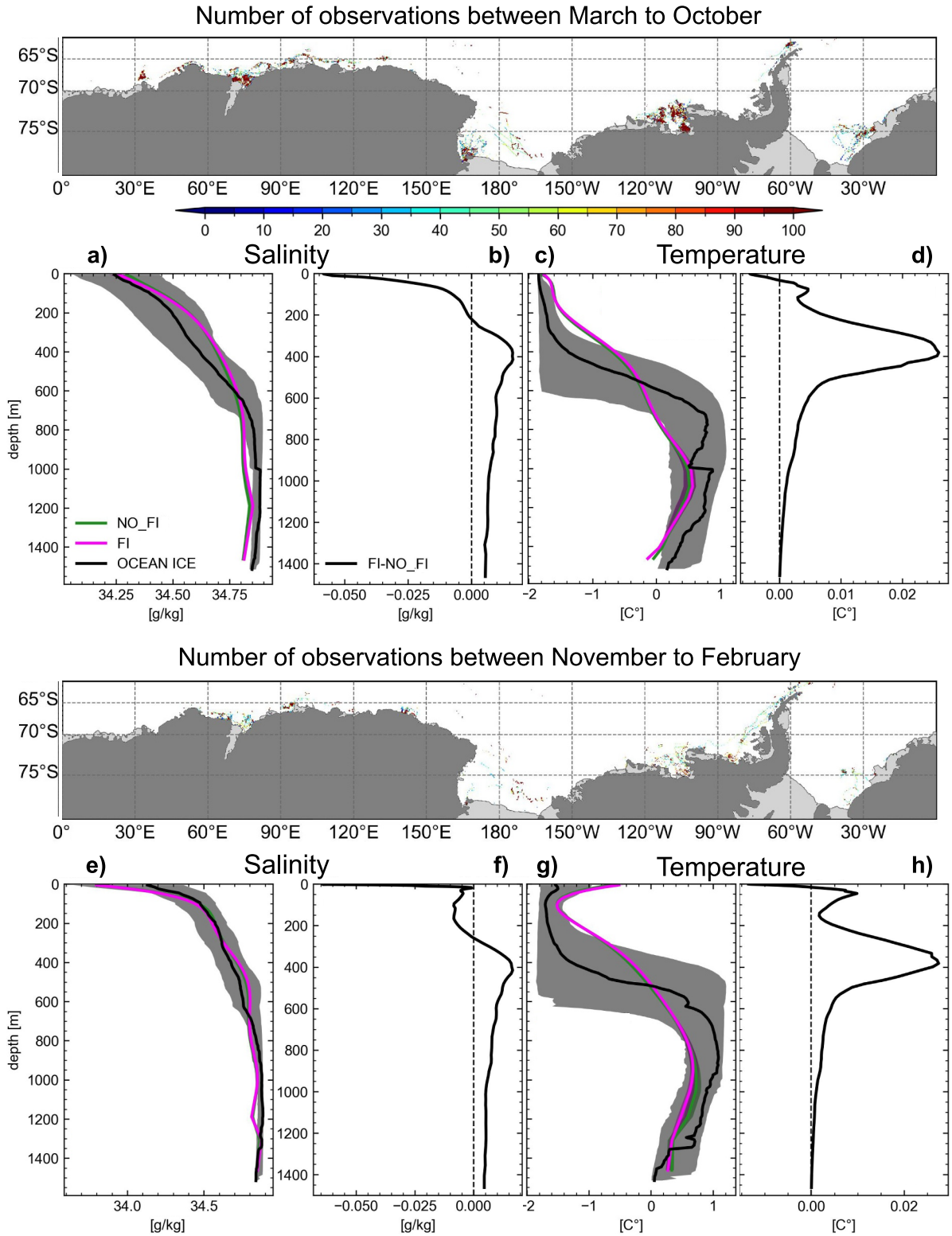



**Figure 3.** Continental shelf 25, 50, and 75 quantiles of temperature and salinity vertical profiles for observations (black) and simulations (FI in pink and NO_FI in green), restricted to grid cells with observations (a, c, e, g). Differences between the two simulations (FI-NO_FI) averaged along the vertical for all continental shelf grid cells (b, d, f, h). Maps show the number of observations in the grid column. The upper part of the figure is for March to October data, while the bottom is for November to February over the period 2013–2017.



21699291, 2026, 10, Downloaded from https://agupubs.onlinelibrary.wiley.com/doi/10.1029/2025JC023673 by Universite Catholique De Louvain, Wiley Online Library on [06/10/2026]. See the Terms and Conditions (https://onlinelibrary.wiley.com/terms-and-conditions) on Wiley Online Library for rules of use; OA articles are governed by the applicable Creative Commons License

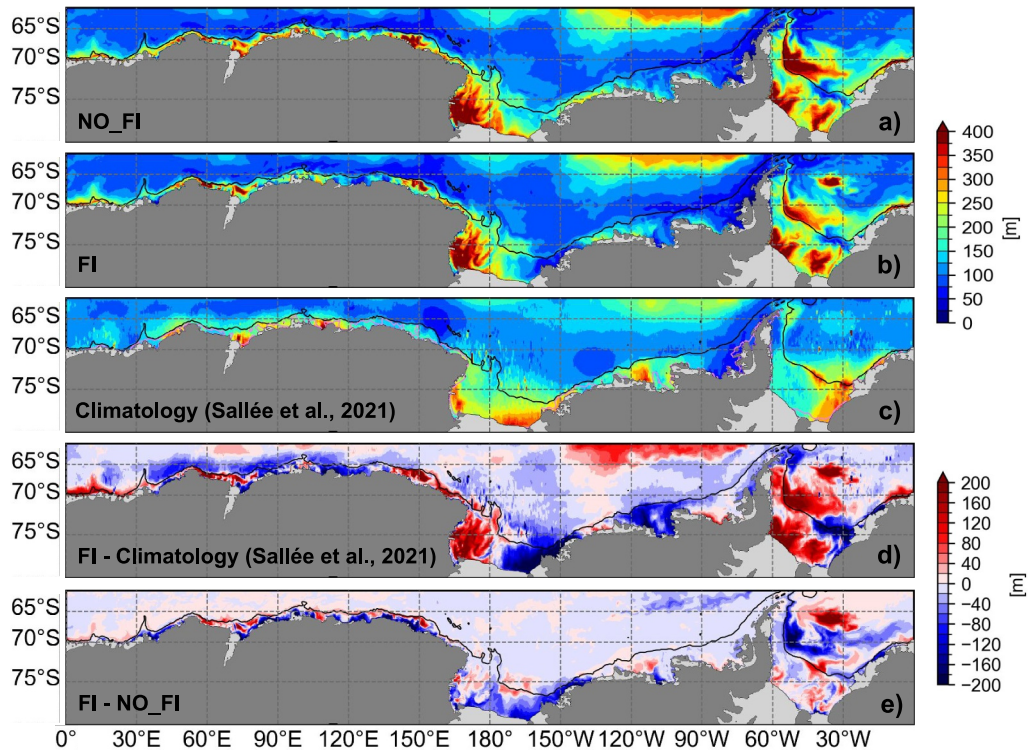



**Figure 4.** Winter mean mixed layer depth (MLD) averaged over July–September (JAS) and the period 2013–2017 from the NO_FI simulation (a), the FI simulation (b), and the observational climatology of Sallée et al. (2021) (c). Differences in winter mean MLD between the FI simulation and the observational climatology (FI-Sallée et al., 2021; d) and between the FI and NO_FI simulations (FI-NO_FI; e). The black contour is the continental shelf border (1,500 m depth). The violet contour in panel (c) indicates the 50% frequency of occurrence of fast ice in the FI simulation over the presented period.

margins. These changes are consistent with the spatial redistribution of the sea ice production noted earlier (Figure 2e). The corresponding map with anomalies incompatible with zero at the 95% confidence interval (Figure S3b in Supporting Information S1) indicates that MLD anomalies within fast ice covered regions reach statistical significance. Another notable change is the dipole anomaly in the open ocean of the western Weddell Sea (Figure 4e). This anomaly is relatively remote from fast ice (Figure 1) and does not coincide with changes in sea ice production (Figure 2). We hypothesize that it is an indirect response involving ocean circulation changes, and possibly increased basal melting of the Larsen C Ice Shelf (see Section 3.5). In the model, this region has a very weak stratification and relatively deep mixed layer (Figure 4b) that are sensitive to small perturbations.

Taken together, Figures 4d and 4e indicate that the velocity-restoring fast ice scheme does not reduce the model MLD biases. Nevertheless, we note that fast ice has a substantial effect over the continental shelf MLD (Figure 4e), with differences exceeding 100 m in some areas, suggesting an important influence on shelf water properties.

### 3.4. Bottom Water Properties

We have seen in the previous sections that representing fast ice in the model importantly influences the simulated geographical distribution of sea ice production and ocean vertical mixing, which are known to influence bottom water mass characteristics. In this section, we assess how these modifications translate into changes in bottom temperature and salinity across the Antarctic continental shelf and explore the processes involved.

#### 3.4.1. Bottom Water Temperature

The FI simulation reproduces reasonably well the large-scale bottom water temperature patterns seen in the WOA18 climatology (Figures 5b and 5c). However, simulated bottom waters are generally too warm off the continental shelf and too cold on the shelf (Figure 5d). There are exceptions, in particular the Ross Ice Shelf



21699291, 2026, 10, Downloaded from https://agupubs.onlinelibrary.wiley.com/doi/10.1029/2025JC023673 by Universite Catholique De Louvain, Wiley Online Library on [06/10/2026]. See the Terms and Conditions (https://onlinelibrary.wiley.com/terms-and-conditions) on Wiley Online Library for rules of use; OA articles are governed by the applicable Creative Commons License

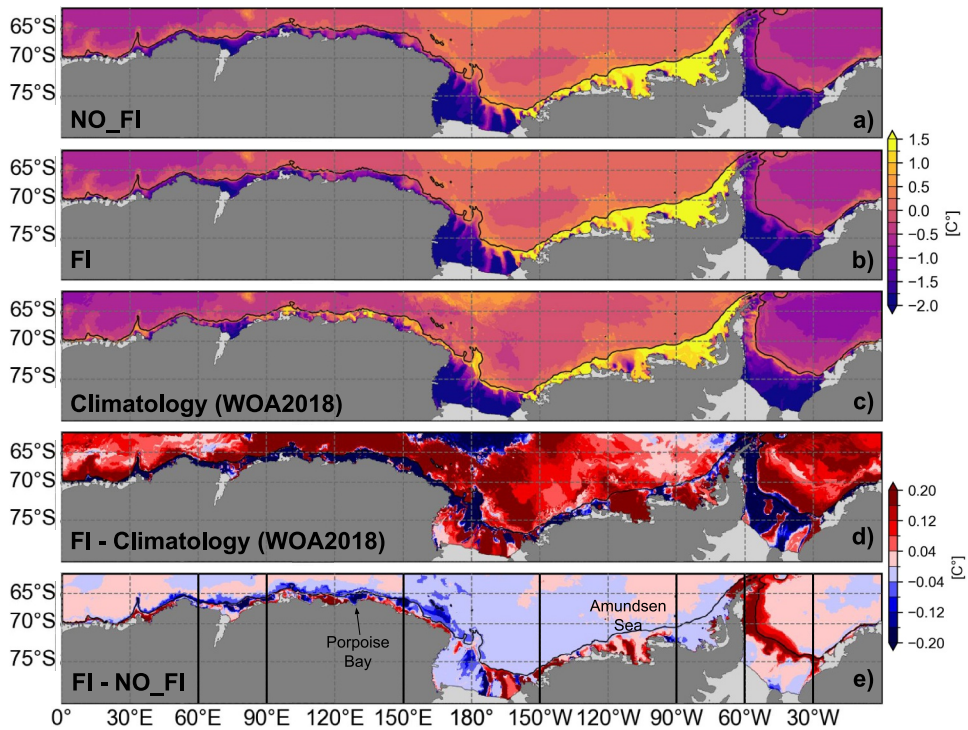



**Figure 5.** Annual mean bottom water temperature averaged over the period 2013–2017 from the NO_FI simulation (a), the FI simulation (b), and the observational climatology of the World Ocean Atlas (WOA2018; c). Differences in annual mean bottom water temperature between the FI simulation and the observational climatology (FI-WOA2018; d) and between the FI and NO_FI simulations (FI-NO_FI; e). The black contour is the continental shelf border (1,500 m depth). Some important locations mentioned in the text and averaging regions delimited with vertical solid black lines are both indicated in panel (e).

margin, the Amundsen Sea, and the Bellingshausen Sea, where the simulated bottom shelf temperature is biased warm by more than 0.2°C (Figure 5d).

Figure 5e indicates that fast ice leads to higher bottom water temperatures along the coast of East Antarctica (+0.13°C on average between 90°E and 150°E), and lower bottom water temperatures further north along the shelf break (−0.11°C on average between 90°E and 150°E). In this region, only part of these anomalies on the shelf exceeds the 95% confidence level (Figure S3c in Supporting Information S1). Notably, pronounced bottom shelf water warming appears along the shelf break of the Weddell Sea extending to the tip of the Antarctic Peninsula (+0.16°C on average between 30°W and 60°W). The whole shelf part of Amundsen Sea is also characterized by higher bottom water temperatures (+0.13°C on average between 90°W and 150°W).

Because the model was initialized with the WOA18 data set (see Section 2.4), the combined analysis of Figures 5d and 5e shows how fast ice changes the bottom water temperature drift from the initial conditions. Representing fast ice results in a modest reduction in the overall discrepancy with WOA18 over the Antarctic continental shelf, as reflected by the slightly lower RMSE in FI (0.231°C) compared with NO_FI (0.236°C). However, some specific regions, including parts of the continental shelf of the Amundsen Sea (~130°W) and Porpoise Bay (~130°E), exhibit larger bottom water temperature drift in FI than in NO_FI. In regions characterized by frequent fast ice or coastal polynyas (>50% frequency of occurrence), the RMSE is also slightly lower in FI (0.895°C) than in NO_FI (0.928°C), indicating a small improvement in the agreement with WOA18. Overall, the response of bottom water temperature to the representation of fast ice is spatially heterogeneous, with relatively small changes compared with the large-scale variability of the temperature field.

### 3.4.2. Bottom Water Salinity

The bottom water salinity pattern simulated in FI is broadly consistent with that of WOA18 (Figures 6b and 6c), but the FI bottom water salinities are generally too low (−0.1 g $kg^{-1}$) over the continental shelf (Figure 6d).



21699291, 2026, 10, Downloaded from https://agupubs.onlinelibrary.wiley.com/doi/10.1029/2025JC023673 by Universite Catholique De Louvain, Wiley Online Library on [06/10/2026]. See the Terms and Conditions (https://onlinelibrary.wiley.com/terms-and-conditions) on Wiley Online Library for rules of use; OA articles are governed by the applicable Creative Commons License

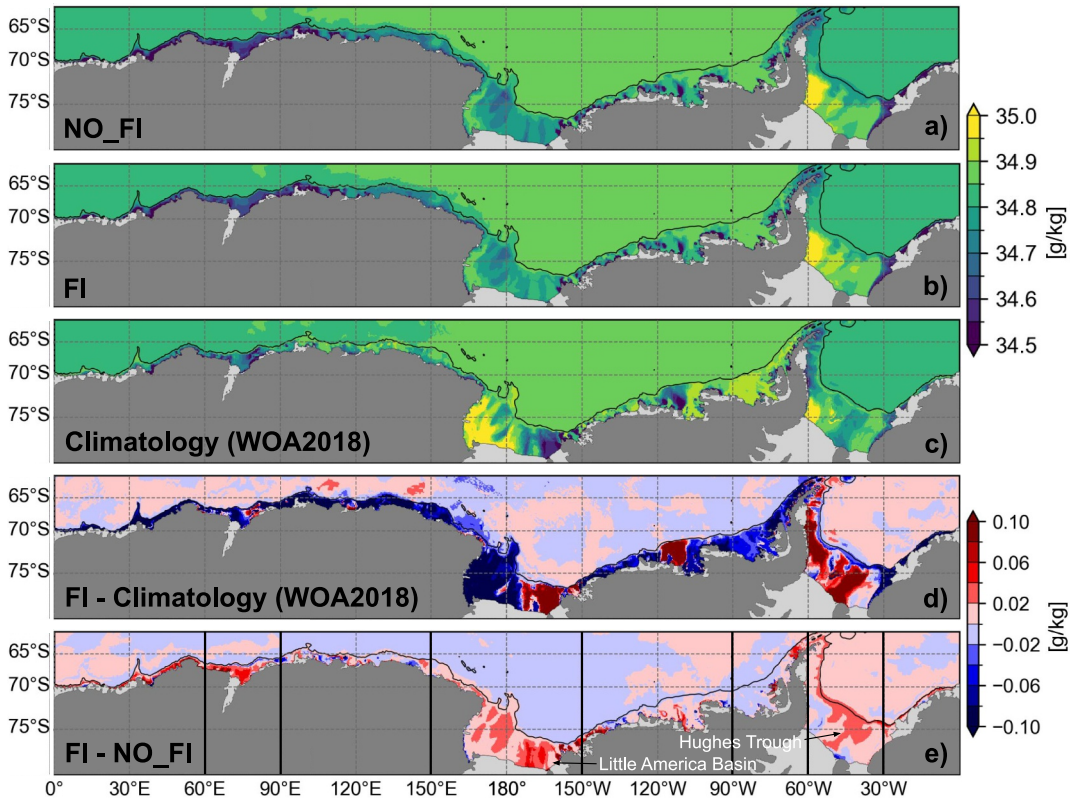



**Figure 6.** Annual mean of bottom water salinity averaged over the period 2013–2017 from the NO_FI simulation (a), the FI simulation (b), and the observational climatology of the World Ocean Atlas (WOA2018; c). Differences in annual mean bottom water salinity between the FI simulation and the observational climatology (FI-WOA2018; d) and between the FI and NO_FI simulations (FI-NO_FI; e). The black contour is the continental shelf border (1,500 m depth). Some important locations mentioned in the text and averaging regions delimited with vertical solid black lines are both indicated in panel (e).

Notable exceptions include the Little America Basin (~160°W), the Dotson-Getz Trough (~110°W), and the Weddell Sea (~50°W), where the model simulates too high salinities (+0.1 g $kg^{-1}$).

As for temperature, Figures 6d and 6e show that incorporating fast ice leads to small changes in the bottom water salinity drift relative to WOA18, with a slight reduction in the overall RMSE over the Antarctic continental shelf (0.039 g $kg^{-1}$ in FI compared with 0.040 g $kg^{-1}$ in NO_FI). The response is spatially heterogeneous, with reduced discrepancies in some regions, including areas characterized by frequent coastal polynya activity, but increased differences in others. For example, larger salinity differences are found in parts of the Little America Basin, the Amundsen Polynya region (~110°W), the Hughes Trough, and off the East Antarctic coast between 90°E and 150°E. In regions with frequent fast ice or coastal polynyas, the RMSE is 0.152 g $kg^{-1}$ in FI compared with 0.158 g $kg^{-1}$ in NO_FI, indicating a fairly small improvement with respect to WOA18. The corresponding map with anomalies (FI-NO_FI) that are incompatible with zero at the 95% confidence interval is displayed in Figure S3d in Supporting Information S1. This figure shows that nearly all bottom water salinity anomalies are statistically significant.

### 3.4.3. Processes Responsible for the Changes in Bottom Water Properties

To understand the mechanisms responsible for the changes in bottom water temperature and salinity identified in Sections 3.4.1 and 3.4.2, we now focus on coastal polynyas areas, where dense water formation occurs. This polynya-scale perspective helps to disentangle the respective roles of surface processes and oceanic circulation in modifying the shelf water properties. In this context, fast ice affects the characteristics of water masses across the continental shelf both directly and indirectly through coastal polynyas.



21699291, 2026, 10, Downloaded from https://agupubs.onlinelibrary.wiley.com/doi/10.1029/2025JC023673 by Universite Catholique De Louvain, Wiley Online Library on [06/10/2026]. See the Terms and Conditions (https://onlinelibrary.wiley.com/terms-and-conditions) on Wiley Online Library for rules of use; OA articles are governed by the applicable Creative Commons License

21699291, 2026, 10, Downloaded from https://agupubs.onlinelibrary.wiley.com/doi/10.1029/2025JC023673 by Universite Catholique De Louvain, Wiley Online Library on [06/10/2026]. See the Terms and Conditions (https://onlinelibrary.wiley.com/terms-and-conditions) on Wiley Online Library for rules of use; OA articles are governed by the applicable Creative Commons License

The direct effects are illustrated in Figure 7, which presents the seasonal cycle of the sea ice concentration and the vertical temperature and salinity anomaly profiles, averaged along a representative transect through the Dalton fast ice region (location shown in Figure 7a, see the solid black line). Figure 7d shows a significant surface salinity reduction in FI compared to NO_FI, with an annual mean change in the upper 50 m of the water column of $-0.51$ g kg$^{-1}$. This freshening leads to a shallower mixed layer in FI (see pink and green lines in Figures 7c and 7d). The difference between the MLDs of the two simulations increases with sea ice production and, therefore, the gap occurs mainly during the ice growth season.

In FI, the modified MLD alters the vertical temperature profile (Figure 7c). In the upper 50 m, a yearlong surface cooling is observed in FI ($-0.2$°C on annual average), attributed to the shallower mixed layer on the shelf, indicative of a more stratified upper ocean, which reduces the mixing of warm deeper waters with the cold surface waters. In agreement with this interpretation, an average warming of 0.2°C is noticed in the ocean layer located between the FI and NO_FI MLDs. This warm subsurface anomaly is maintained throughout the sea ice growth season and decays in summer with the decrease of the gap between the two simulated MLDs. Because mixing and cooling of subsurface waters can be stronger in coastal polynyas, we examined whether part of the shown FI-NO_FI subsurface temperature difference may reflect polynya-driven convection in NO_FI rather than a direct effect of fast ice in FI. During the period of subsurface warming both simulations show high sea ice concentration (more than 75%) in this region (Figure 7b), indicating that there is no active polynya in the region in NO_FI. The warming therefore primarily reflects reduced vertical mixing under fast ice covered conditions relative to pack ice conditions.

During summer, we see a net average cooling of the upper 100 m of the water column by about $-0.7$°C in FI relative to NO_FI (Figure 7c). We argue that this temperature difference results from the locally larger sea ice concentration in the FI simulation (Figure 7b), reducing shortwave radiation supply and wind-induced mixing in the upper ocean. Indeed, more sea ice increases the surface albedo and thereby reduces the absorption of incoming solar radiation. Because shortwave radiation in NO_FI can penetrate at depth, in particular below the stratified surface layer, and not in FI, the span of relatively cold waters in FI reaches the bottom of the continental shelf. This temperature difference explains the bottom water temperature decrease in the Dalton Polynya region (Figure 5e; Porpoise Bay). The presence of sea ice in FI also reduces wind-driven mixing and contributes to maintaining a colder and more stratified upper ocean. Furthermore, while sea ice is present, a large part of the thermal energy available in the upper ocean is consumed by melting sea ice, which limits the amount of heat available to warm the ocean surface. The sensible heat flux associated with the release of the associated melt water is about 1 W m$^{-2}$ and therefore is negligible compared to $\mathcal{O}(10^2$ W m$^{-2})$ associated with shortwave radiation. In contrast, most of the continental shelf regions close to the coast exhibit a bottom water warming. This warming is linked to the difference between the two simulated MLDs: in those regions, unlike in the Dalton Polynya region, the MLD in NO_FI reaches the seafloor such that the positive temperature anomaly between the two MLDs extends to the bottom. This mechanism is particularly evident in the Dibble Polynya region (Figure S6 in Supporting Information S1).

We also find differences caused by reduced melting, but they are smaller than ice-production-induced differences. The vertical ice-ocean mass flux averaged over NDJF (i.e., the sea ice melt season) and integrated over the region with more than 50% fast ice frequency of occurrence during NDJF is reduced by 15% relative to NO_FI ($-0.065$ kg m$^{-2}$ s$^{-1}$). This is consistent with the presence of thicker and more persistent fast ice in the FI simulation (see Pirlet et al., 2025), which limits summer break-up and reduces meltwater release. Enhanced upper-ocean stratification also contributes by maintaining colder surface waters. In contrast, the difference in the integrated vertical ice-ocean mass flux is substantially larger during the sea ice growth season ($-49$% relative to NO_FI; $-0.394$ kg m$^{-2}$ s$^{-1}$), indicating that the freshwater signal associated with reduced summer melt is of secondary importance compared to the impact of reduced sea ice production and associated brine rejection beneath fast ice. This is consistent with the simulated salinity anomalies in the Dalton region (Figure 7d), which show water salinity reduction in FI throughout the year.

Now we examine the indirect effect of fast ice on shelf water properties through its impact on coastal polynyas. The Dalton Polynya (Figure 7a) exhibits a reduction in sea ice production beneath fast ice (Figure 8a) and a decrease in surface and subsurface salinity in the downstream polynya (Figure 8c). We argue that ocean surface currents, indicated by arrows in Figure 8b, transport fresher waters from the fast ice region toward the polynya. To quantify this transport of fresher waters, we computed the integrated salt transport across a section located

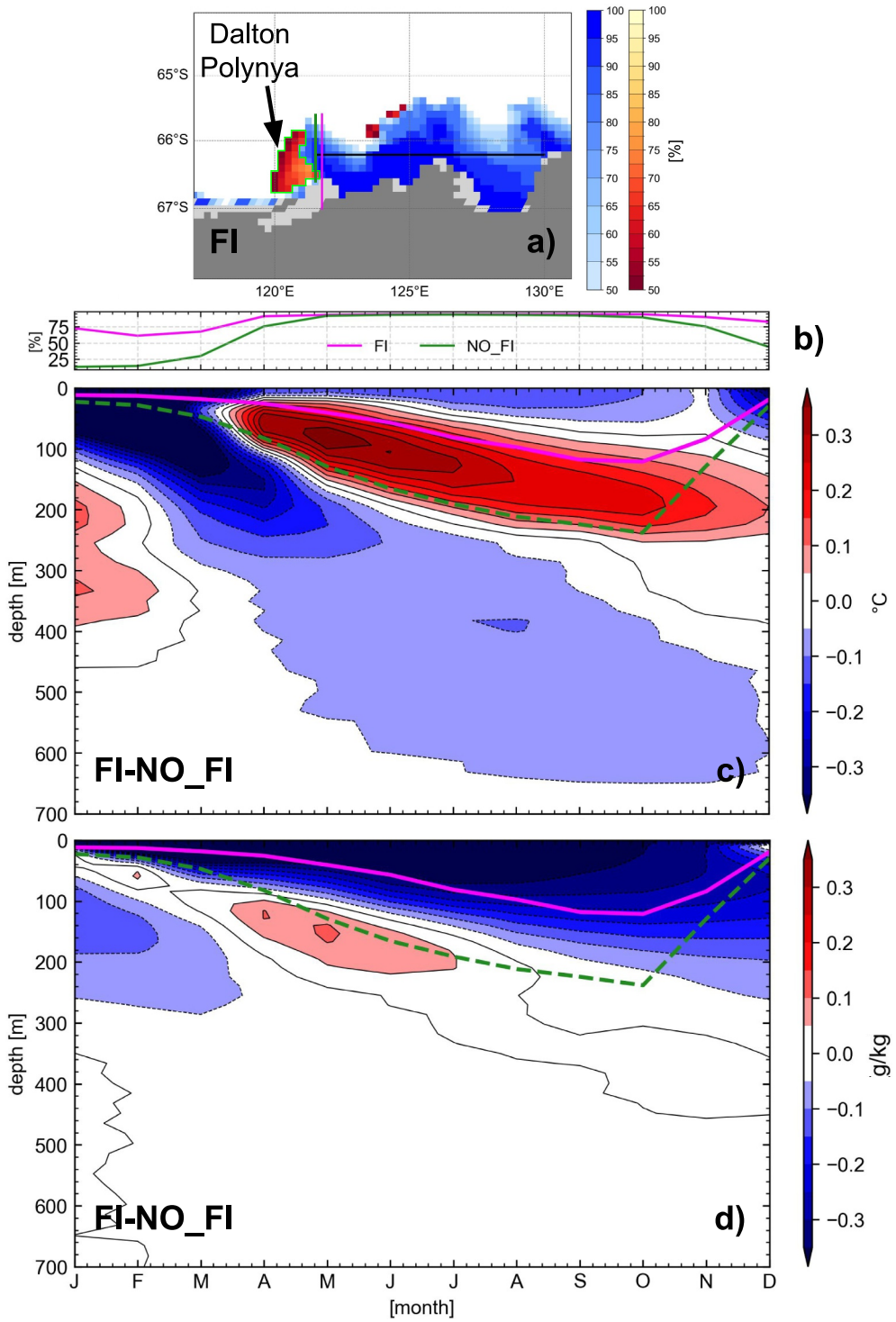



**Figure 7.** (a) Frequency of occurrence of coastal polynyas (orange shading) and fast ice (blue shading) averaged over March–October and the period 2013–2017 in the Dalton Polynya region from the FI simulation. The black line indicates the fast ice transect used for the analyses shown in panels (b–d) and in Figures 10b and 10d. The green section shows the location of the vertical cross section (surface-50 m depth) across which the freshwater flux advected from beneath the fast ice tongue toward the coastal polynya is calculated, while the pink section indicates the transect used for the latitude-depth analysis presented in Figures 10a and 10c. (b) Seasonal cycles of sea ice concentration along the transect shown in panel (a) averaged over 2013–2017 for FI and NO_FI simulations. (c, d) Monthly climatology of temperature and salinity anomalies, respectively, shown as depth-time (Hovmöller) diagrams and averaged along the fast ice transect. The seasonal cycle of the mean mixed layer depth in the transect for FI (solid pink line) and for NO_FI (dashed green line) is also shown in panels (c, d).



21699291, 2026, 10, Downloaded from https://agupubs.onlinelibrary.wiley.com/doi/10.1029/2025JC023673 by Universite Catholique De Louvain, Wiley Online Library on [06/10/2026]. See the Terms and Conditions (https://onlinelibrary.wiley.com/terms-and-conditions) on Wiley Online Library for rules of use; OA articles are governed by the applicable Creative Commons License

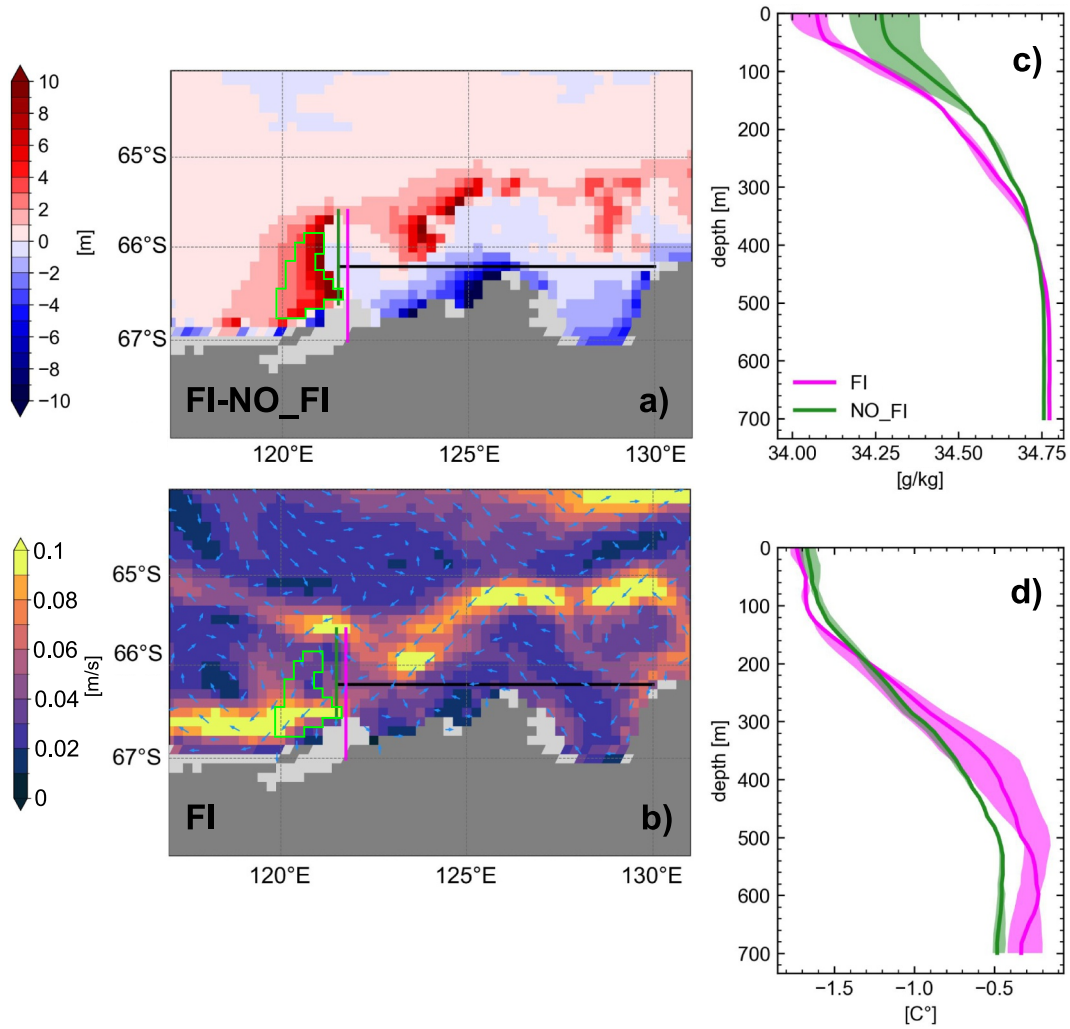



**Figure 8.** (a) Mean sea ice production anomaly (FI-NO_FI) in the Dalton Polynya region averaged over March–October for 2013–2017. The solid black line indicates the longitude-depth transect analysed in Figures 7, 10b, and 10d, while the pink section is used for the latitude-depth analysis presented in Figures 10a and 10c. (b) Mean ocean current velocity and direction averaged over the upper 50 m in the FI simulation for the same period as in panel (a). The solid green line in panels (a, b) shows the location of the vertical section (0–50 m depth) across which the freshwater flux advected from beneath the fast ice tongue toward the coastal polynya is calculated. (c, d) Vertical salinity and temperature profiles, respectively, from the FI and NO_FI simulations averaged over the region enclosed by the green contour shown in panels (a, b) and over March–October for 2013–2017. Shading indicates the range between the 25th and the 75th quantiles.

between the fast ice tongue and the coastal polynya (Figures 7a, 8a, and 8b; solid green line), extending vertically from the surface to 50 m depth in both simulations. The net salt transport across this section is directed toward the polynya in both simulations but is weaker in FI (4.2 g $kg^{-1}$ Sv) than in NO_FI (13.2 g $kg^{-1}$ Sv). This reduced salt transport in FI compared to NO_FI, through the section, is consistent with a diminished export of saline water from the fast ice region, supporting the interpretation that fresher surface waters are advected into the downstream polynya. Temperature profiles reveal a cooling in the upper 200 m, associated with the open coastal polynya in FI, while a warming is observed at depth. Note that a similar surface freshening also occurs in other coastal polynyas influenced by upstream fast ice coverage, including the Amundsen, Dibble, Shackleton, Vincennes Bay, and Mertz Polynyas (Figures S9–S13 in Supporting Information S1).

In contrast, other polynyas, such as the Cape Darnley Polynya, exhibit a different behavior due to limited presence of upstream fast ice tongue. Figure 9a provides a detailed view of the frequency of occurrence of the Cape Darnley Polynya together with the adjacent fast ice. Figure 9b, which presents the mean sea ice production anomaly



21699291, 2026, 10, Downloaded from https://agupubs.onlinelibrary.wiley.com/doi/10.1029/2025JC023673 by Universite Catholique De Louvain, Wiley Online Library on [06/10/2026]. See the Terms and Conditions (https://onlinelibrary.wiley.com/terms-and-conditions) on Wiley Online Library for rules of use; OA articles are governed by the applicable Creative Commons License

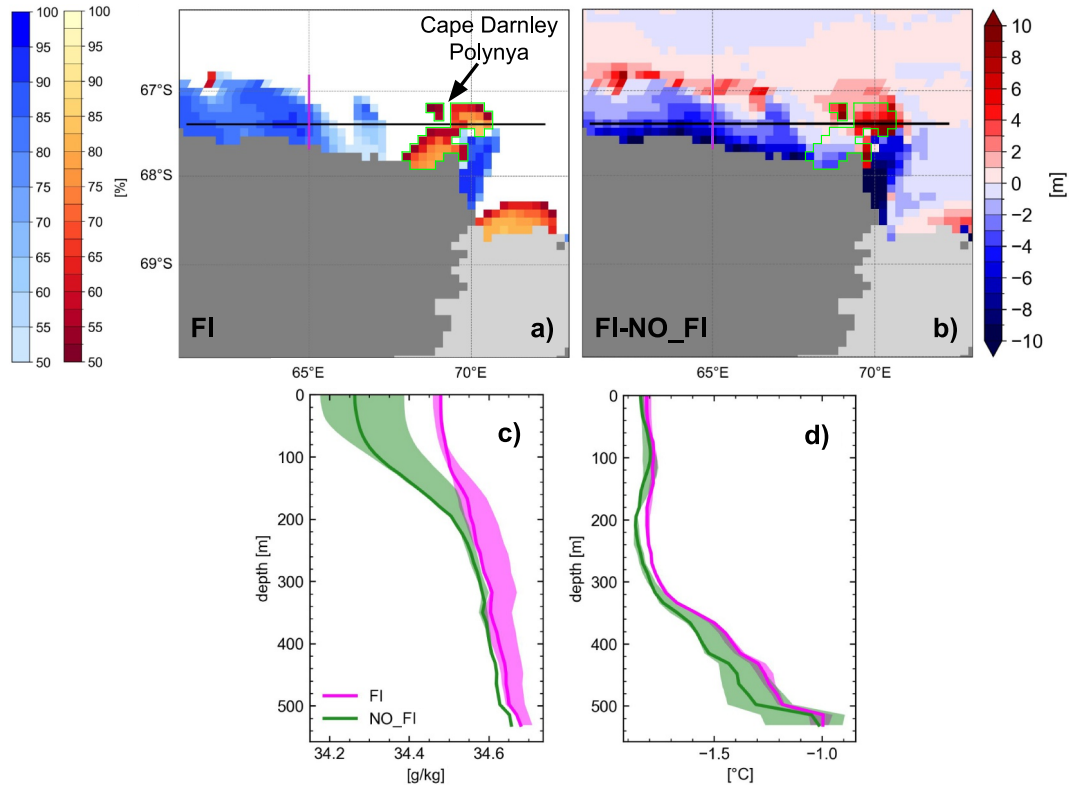



**Figure 9.** (a) Frequency of occurrence of coastal polynyas (orange shading) and fast ice (blue shading) averaged over March–October and the period 2013–2017 in the Cape Darnley and Mackenzie Bay region from the FI simulation. The solid black and pink line sections are used, respectively, for longitude-depth and latitude-depth analysis presented in Figures 10e, 10f, 10g, and 10h. (b) Mean sea ice production anomaly (FI-NO_FI) in the region averaged over March–October for 2013–2017. (c, d) Vertical salinity and temperature profiles, respectively, from the FI and NO_FI simulations averaged over the region enclosed by the green contour shown in panels (a, b) and over March–October for 2013–2017. Shading indicates the range between the 25th and the 75th quantiles.

(FI-NO_FI), reveals enhanced sea ice production within the coastal polynya in the FI simulation and a reduced sea ice production beneath fast ice. Figures 9c and 9d show the corresponding vertical profiles of salinity and temperature averaged in the Cape Darnley Polynya (see the green contour in Figures 9a and 9b). The representation of fast ice results in a marked salinity increase in the upper 200 m of the polynya water column, driven by increased ice production and associated brine rejection. Below 200 m, the salinity anomaly decreases. In FI, the reduced halocline strengths vertical exchanges between the surface and bottom layers (Figure 9c), allowing the surface salt accumulation to reach the seabed more effectively. In contrast, the impact of fast ice on temperature remains small throughout the water column in this coastal polynya (Figure 9d). Similar surface salinity increases are observed in other key polynyas, including the Mackenzie Bay Polynya and to a lesser extent the Terra Nova Bay Polynya (Figures S7 and S8 in Supporting Information S1).

Having examined the direct and indirect effects of fast ice, we now investigate how surface anomalies are transmitted to the subsurface, bottom waters, and under ice shelf cavities. Figure 10 depicts latitude-depth and longitude-depth sections of annual mean temperature and salinity anomalies (FI-NO_FI) in the Dalton and Cape Darnley regions.

In the Dalton region, the representation of fast ice produces colder and mainly fresher surface waters (Figures 10b and 10d), which shoal the mixed layer. The reduced vertical mixing allows warmer and saltier waters intrusion onto the continental shelf (Figures 10a–10d). The latitude-depth section extending beneath the Totten Ice Shelf (Figures 10a and 10c) further shows that these subsurface warmer and saltier waters penetrate into the ice shelf cavity.



21699291, 2026, 10, Downloaded from https://agupubs.onlinelibrary.wiley.com/doi/10.1029/2025JC023673 by Universite Catholique De Louvain, Wiley Online Library on [06/10/2026]. See the Terms and Conditions (https://onlinelibrary.wiley.com/terms-and-conditions) on Wiley Online Library for rules of use; OA articles are governed by the applicable Creative Commons License

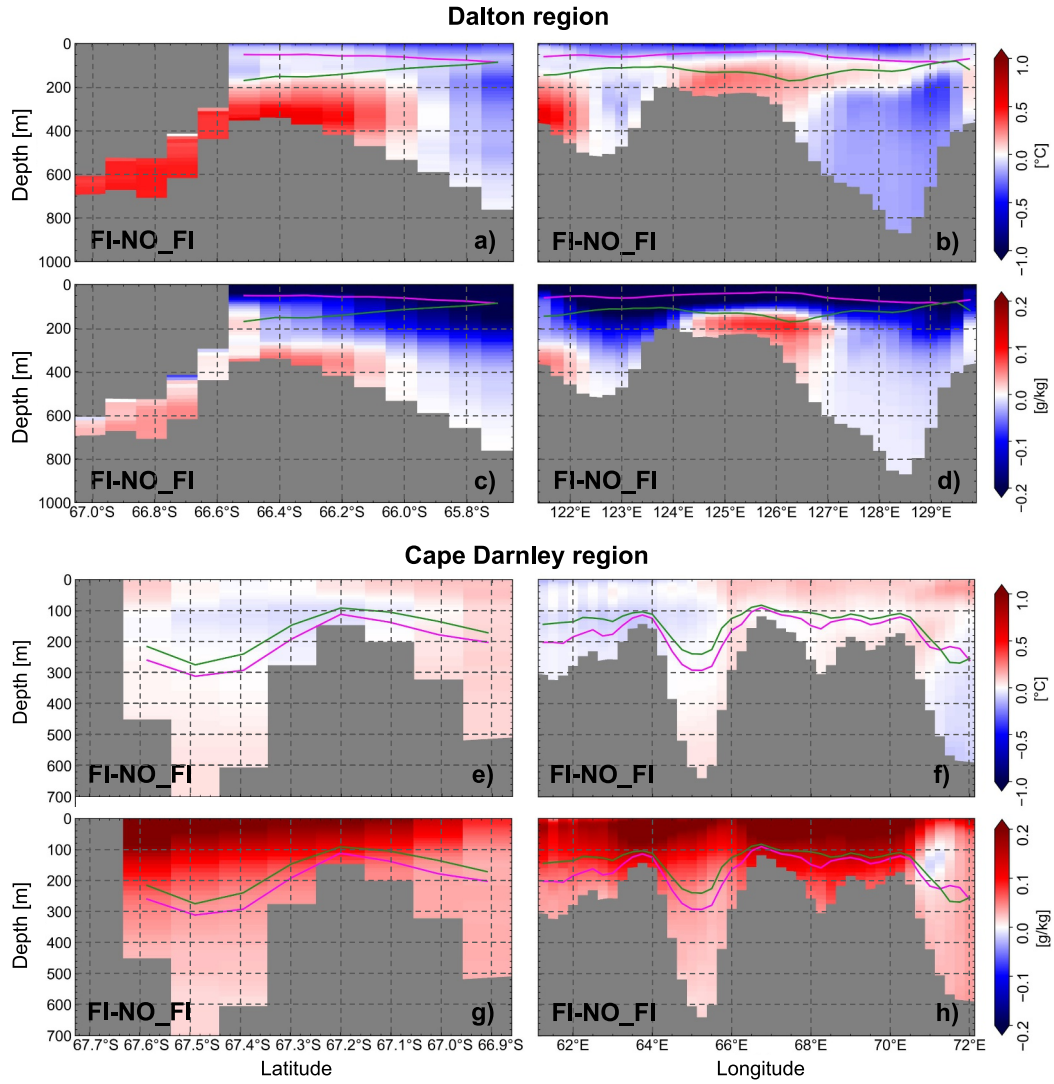



**Figure 10.** Transects of the annual mean water temperature anomalies (FI-NO_FI; a, b, e, f) and salinity anomalies (FI-NO_FI; c, d, g, h) averaged over the period 2013–2017 in the Dalton (a–d) and Cape Darnley (e–h) regions. The locations of these sections are indicated in Figures 7a and 9a for the Dalton and Cape Darnley regions, respectively, where the latitude-depth sections (a, c, e, g) are shown in pink and the longitude-depth sections (b, d, f, h) in black. The annual mean mixed layer depth averaged over 2013–2017 is overlaid in all panels for the NO_FI simulation (solid green line) and the FI simulation (solid pink line).

In contrast, the Cape Darnley region exhibits increased surface salinity, including beneath fast ice (Figure 10h), which can be traced to the Cape Darnley Polynya (Figures 9a and 9c), the primary source of dense water in the region. We argue that the salinity increase has a local coastal origin rather than an offshore source: (a) it is confined to the coastal zone (Figure 10g), and (b) the associated density increase deepens the mixed layer, further limiting the intrusion of saline waters beneath the fast ice. In this framework, enhanced sea ice production in the Cape Darnley Polynya generates dense waters that are advected westward along the continental shelf, contributing to the downstream salinity increase from the surface to the bottom of the shelf. This interpretation is consistent with the bottom water salinity anomalies shown in Figure 6e, which reveal saltier waters both at the polynya location and downstream. Temperature changes (Figures 10e and 10f) are comparatively small but also reflect the downstream advection of waters originating from the Cape Darnley Polynya.

The representation of fast ice can also have remote effects on bottom temperature and salinity via changes in ocean circulation and stratification that reorganize water masses. This appears to be the case along the shelf break in the northwestern Weddell Sea, where bottom waters are warmer and slightly saltier in FI than NO_FI



21699291, 2026, 10, Downloaded from https://agupubs.onlinelibrary.wiley.com/doi/10.1029/2025JC023673 by Universite Catholique De Louvain, Wiley Online Library on [06/10/2026]. See the Terms and Conditions (https://onlinelibrary.wiley.com/terms-and-conditions) on Wiley Online Library for rules of use; OA articles are governed by the applicable Creative Commons License

21699291, 2026, 10, Downloaded from https://agupubs.onlinelibrary.wiley.com/doi/10.1029/2025JC023673 by Universite Catholique De Louvain, Wiley Online Library on [06/10/2026]. See the Terms and Conditions (https://onlinelibrary.wiley.com/terms-and-conditions) on Wiley Online Library for rules of use; OA articles are governed by the applicable Creative Commons License

(Figures 5e and 6e). We hypothesize that this signal is linked to reduced wintertime deep convection (cf. decreased MLDs, Figure 4e) and a shoreward expansion of CDW.

### 3.5. Ice Shelf Basal Melt

Figure 11 displays the average integrated basal melt rate of a selection of Antarctic ice shelves, either adjacent to fast ice (see the stars in Figure 11) or among the largest in area (Table S1 in Supporting Information S1 gives the melt rate of all ice shelves) for both FI and NO_FI simulations together with observation-based estimates. Both simulations produce total ice shelf melt rates above estimates (1,264 ± 147 Gt yr $^{-1}$ in Adusumilli et al. (2020); 1,325 ± 237 Gt yr $^{-1}$ in Rignot et al. (2013); 1,082 ± 111 Gt yr $^{-1}$ in Davison et al. (2023)), with values of 1,607 Gt yr $^{-1}$ (NO_FI) and 1,861 Gt yr $^{-1}$ (FI). A substantial part of this positive bias originates from individual ice shelves (e.g., George VI), and is consistent with the broader Southern Ocean warm bias visible in bottom temperatures (Figure 5d). In addition, basal melt estimates are known to be highly sensitive to parameterization choices and the uppermost grid resolution beneath the ice shelf (Gwyther et al., 2020), making perfect agreement with observations difficult to achieve. In this context, the contribution of the present study is not to optimize agreement with estimates of ice shelf melt rates, but rather to show how fast ice can influence ice shelf melting.

The FI-NO_FI difference corresponds to an increase of 254 Gt yr $^{-1}$ (+15.8%) of the integrated ice shelf melt rate. This increase is primarily associated with warmer continental shelf waters in the vicinity of ice shelves under fast ice conditions, as illustrated in Figures 5e and 7c. The magnitude of this change is of the same order as the spread in current observation-based estimates of Antarctic ice shelf melt.

Furthermore, this difference in ice shelf basal melt rate is incompatible with zero at the 95% confidence interval ($t$-test, $p < 0.001$) and exceeds the model's interannual variability. The fast ice induced change in ice shelf melt rate is 3.4–6.4 times larger than the typical interannual fluctuations, which are about 75 Gt yr $^{-1}$ in NO_FI and 40 Gt yr $^{-1}$ in FI. This indicates that the response to fast ice representation constitutes a robust shift in the Antarctic ice shelf melt rate rather than a manifestation of internal variability.

Individually, a few small ice shelves along East Antarctica, as well as the Abbot Ice Shelf, exhibit reductions in basal melt rates. However, none of these decreases exceeds 36% (Holmes). In contrast, the majority of ice shelves experience increased basal melting when fast ice is represented, with most of these changes being non-negligible. Notably, the Moscow University, Totten, Nickerson, and Ross Ice Shelves show increases exceeding 50%. Previous work by Van Achter, Fichefet, Goosse, and Moreno-Chamarro (2022) already mentions an increased melting of the Moscow University and Totten Ice Shelves due to inclusion of fast ice. They attributed this feature to enhanced intrusions of mCDW (modified CDW), facilitated by the presence of fast ice. Similarly, the increase of ice shelf melting in our FI simulation is explained by subsurface warming (Figures 10a and 10b), itself driven by increased near-surface haline stratification and mixed layer thinning. The ice shelves for which significant changes in basal melt coincide with the presence of surrounding fast ice are marked with cyan stars in Figure 11.

### 3.6. Shelf Water Density

Figures 12b and 12c shows that the large-scale patterns of the bottom water potential density mapped from the WOA18 climatology are relatively well preserved in the FI simulation. The comparison between the FI and NO_FI simulations (Figure 12e) reveals a small average bottom density difference over the continental shelf of +0.0007 kg m$^{-3}$ in FI, but spatial variability is evident, with some areas displaying local pronounced anomalies. To isolate the most significant changes (Figure S3e in Supporting Information S1), we only keep anomalies incompatible with zero at the 95% confidence interval which are outside the ±0.02 kg m$^{-3}$ range and identified five sectors of interest (Figure 12e): the Weddell Sea Sector (WSS), the Cape Darnley Sector (CDS; defined here as a sector of DSW production that includes the Cape Darnley polynyas as well as Prydz Bay and the Amery Ice Shelf region), the East Antarctic Sector (EAS), the Ross Sea Sector (RSS), and the Amundsen Sea Sector (ASS). The first four of these sectors include known areas of DSW formation.

In the CDS (50°E to 90°E), the bottom water density increases on average by 0.040 kg m$^{-3}$ in FI. This region is known for the formation of dense water associated with the high activity of the Cape Darnley and Mackenzie Bay Polynyas (Ohshima et al., 2013; Williams et al., 2016). In our simulation, the representation of fast ice leads to an overall increase in bottom water salinity (Figure 6e), driven by enhanced sea ice production in these two key coastal polynyas (Figure 2e). In FI, the increased brine rejection in coastal polynya facilitates vertical salinity

10.1029/2025JC023673

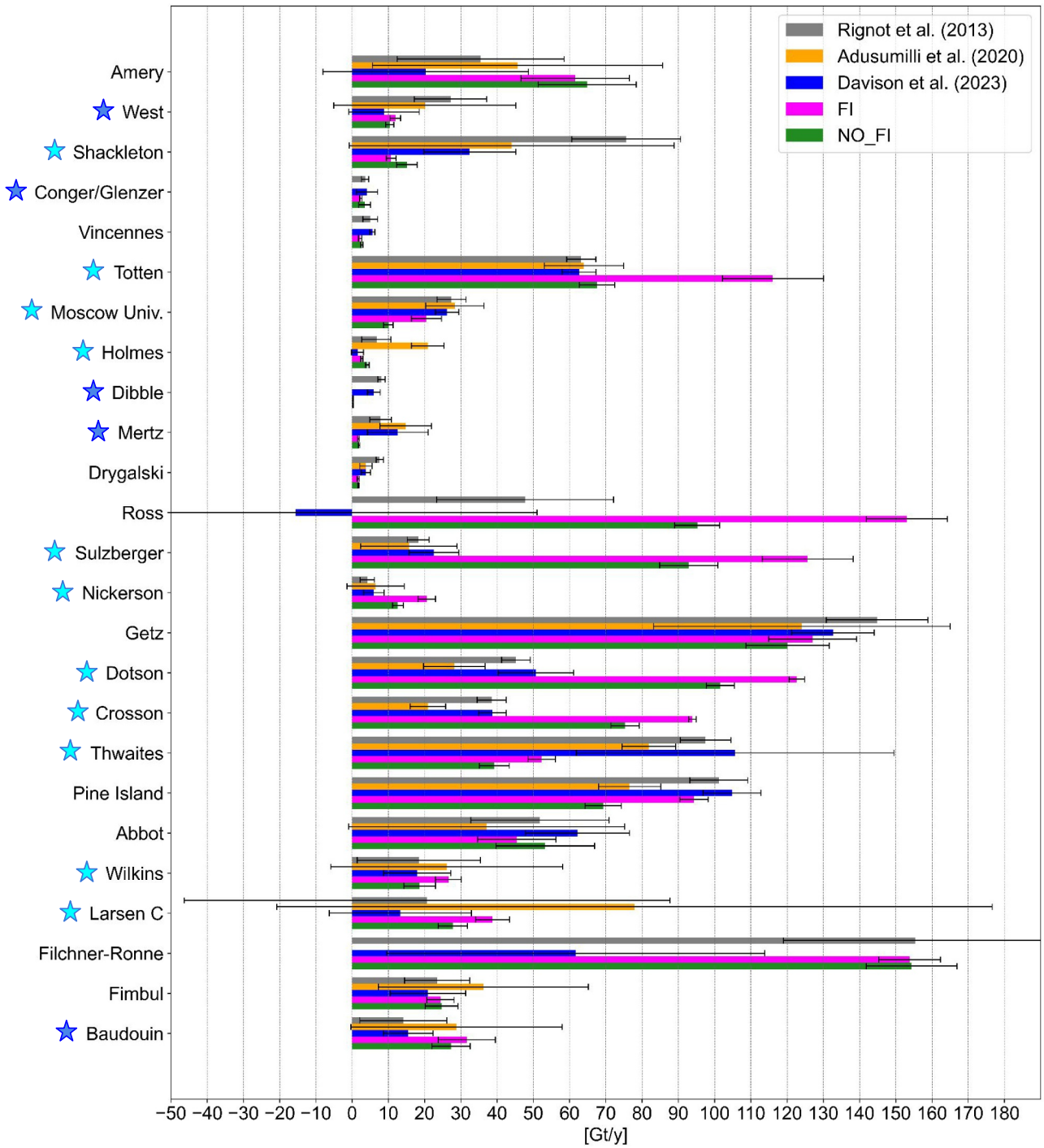



**Figure 11.** Integrated basal melt rate of individual ice shelves in FI (pink) and NO_FI (green) simulations (in Gt $yr^{-1}$), averaged over the period 2013–2017. The observation-based estimates from Rignot et al. (2013), Adusumilli et al. (2020), and Davison et al. (2023) are given in gray, orange, and blue, respectively. The error bars indicate interannual standard deviation. A star means that the ice shelf is close to a fast tongue and, if the star is in cyan, the uncertainties do not overlap. Figure 1 of Rignot et al. (2013) shows the locations of individual selected ice shelves.



21699291, 2026, 10, Downloaded from https://agupubs.onlinelibrary.wiley.com/doi/10.1029/2025JC023673 by Universite Catholique De Louvain, Wiley Online Library on [06/10/2026]. See the Terms and Conditions (https://onlinelibrary.wiley.com/terms-and-conditions) on Wiley Online Library for rules of use; OA articles are governed by the applicable Creative Commons License

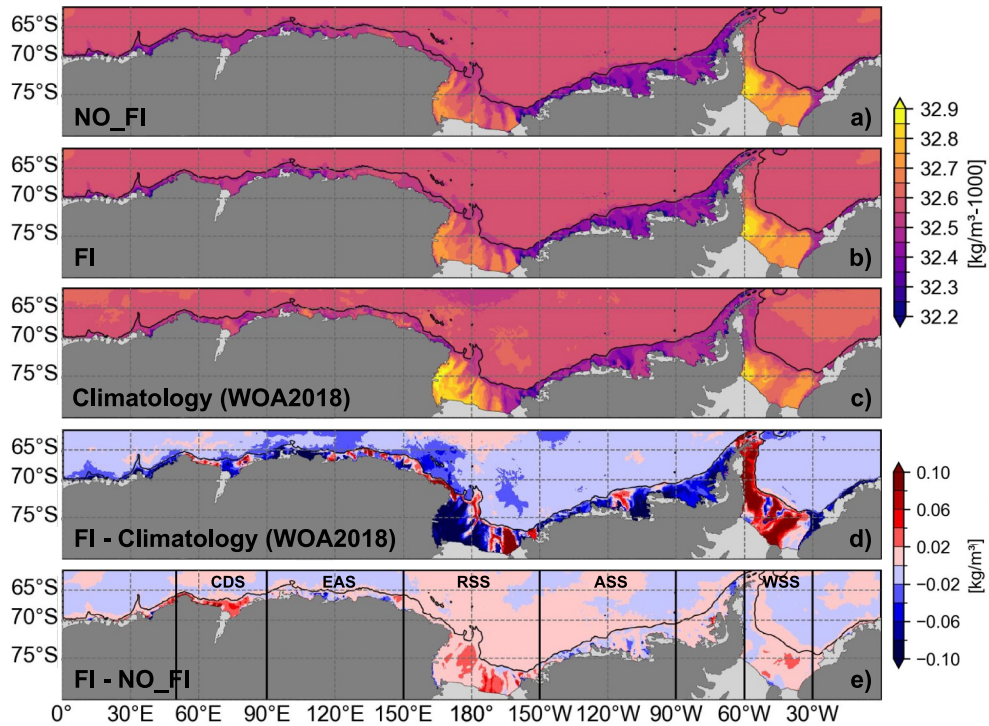



**Figure 12.** Annual mean bottom water density with reference pressure of 1,000 dbar averaged over the period 2013–2017 from the NO_FI simulation (a), the FI simulation (b), and the observational climatology of the World Ocean Atlas (WOA2018; c). Differences in annual mean bottom water density between the FI simulation and the observational climatology (FI-WOA2018; d) and between the FI and NO_FI simulations (FI-NO_FI; e). The black contour is the continental shelf border (1,500 m depth) and black vertical lines are the limits of each sector presented in the Section 3.6: Cape Darnley Sector (50°E–90°E), East Antarctic Sector (90°E–150°E), Ross Sea Sector (150°E–150°W), Amundsen Sea Sector (150°W–90°W), and Weddell Sea Sector (60°W–30°W).

fluxes to the seafloor (Figure 9c), and the resulting salinity signal is subsequently redistributed across the shelf through advective and diffusive processes. Figure 13a confirms a volumetric shift toward denser shelf waters in the FI simulation, with most of the positive volume differences concentrated near freezing temperatures and salinities exceeding 34.6 g $kg^{-1}$, consistent with HSSW formation (Miller et al., 2024). These results emphasize the importance of fast ice representation for the correct simulation of dense water formation in the CDS.

Along the EAS (90°E to 150°E), the bottom water density decreases by 0.020 kg $m^{-3}$ on average in FI compared to NO_FI. Although fast ice allows the formation of coastal polynyas in the model (Figure 1), most of the region experiences a bottom water density decrease linked to local changes, namely bottom shelf water warming (Figure 5e) and freshening beneath the fast ice cover. Additionally, Figure 13b shows a greater volume in FI of cold waters below the freezing point (i.e., ISW), which results from increased ice shelf basal melting in this sector (Figure 11). HSSW formation in this sector typically occurs in the Mertz Polynya (Adélie Depression; Martin et al., 2017; G. Williams & Bindoff, 2003; Williams et al., 2008, 2016) and, to a lesser extent, in Vincennes Bay (Kitade et al., 2014). A localized increase in bottom water density is found downstream of the Mertz Depression (Figure 12e), consistent with the Ninnis Glacier Polynya improved representation in the FI simulation, while a decrease in bottom water density is found beneath the fast ice downstream of the Mertz polynya. In contrast, changes around Vincennes Bay remain limited between FI and NO_FI. Overall, fast ice representation leads to the consumption of mCDW to form DSW in this region (Figure 13b) and a new volume of AASW is also formed due to the surface freshening under fast ice. These findings are consistent with those for the Terre Adélie coastal region reported by Huot et al. (2022).

In the RSS (150°E to 150°W), representing fast ice leads to a bottom water density increase of 0.017 kg $m^{-3}$ on average in FI compared to NO_FI. In this sector, HSSW is known to be formed in the Terra Nova Bay and Ross Ice Shelf Polynyas, while ISW originates from basal melting of the Ross Ice Shelf. Intrusions of mCDW via



21699291, 2026, 10, Downloaded from https://agupubs.onlinelibrary.wiley.com/doi/10.1029/2025JC023673 by Universite Catholique De Louvain, Wiley Online Library on [06/10/2026]. See the Terms and Conditions (https://onlinelibrary.wiley.com/terms-and-conditions) on Wiley Online Library for rules of use; OA articles are governed by the applicable Creative Commons License

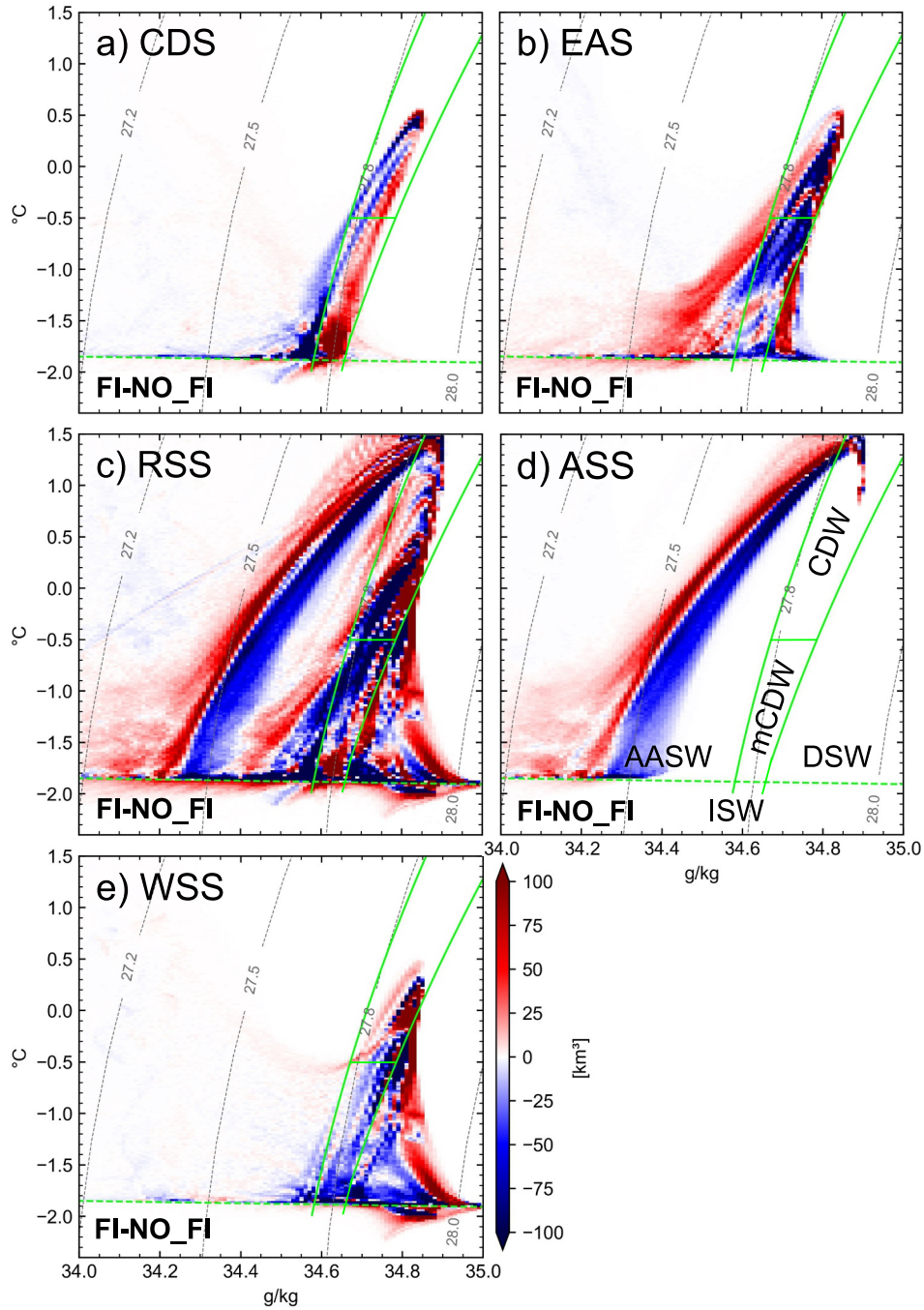



**Figure 13.** Differences (FI-NO_FI) in volume distributions of water masses (bin widths: 0.02°C and 0.01 g $kg^{-1}$) as a function of temperature and salinity for (a) the Cape Darnley Sector (50°E–90°E), (b) the East Antarctic Sector (90°E–150°E), (c) the Ross Sea Sector (150°E–150°W), (d) the Amundsen Sea Sector (150°W–90°W) and (e) the Weddell Sea Sector (60°W–30°W). Volume distributions exclude grid cells located underneath the ice shelves and seaward of the 1,500 m bathymetric contour. Dotted gray curves: potential density referenced to the surface. Solid green curves: neutral density (Jackett & Mcdougall, 1997) values 28 and 28.27. Dashed green line: surface freezing temperature. AASW: Antarctic Surface Water, CDW: Circumpolar Deep Water, mCDW: modified CDW, DSW: Dense Shelf Water are presented in panel (d). The water mass classification is based on Herraiz-Borreguero et al. (2015), Herraiz-Borreguero et al. (2016), Williams et al. (2016), and A. H. Orsi and Wiederwohl (2009).



21699291, 2026, 10, Downloaded from https://agupubs.onlinelibrary.wiley.com/doi/10.1029/2025JC023673 by Universite Catholique De Louvain, Wiley Online Library on [06/10/2026]. See the Terms and Conditions (https://onlinelibrary.wiley.com/terms-and-conditions) on Wiley Online Library for rules of use; OA articles are governed by the applicable Creative Commons License

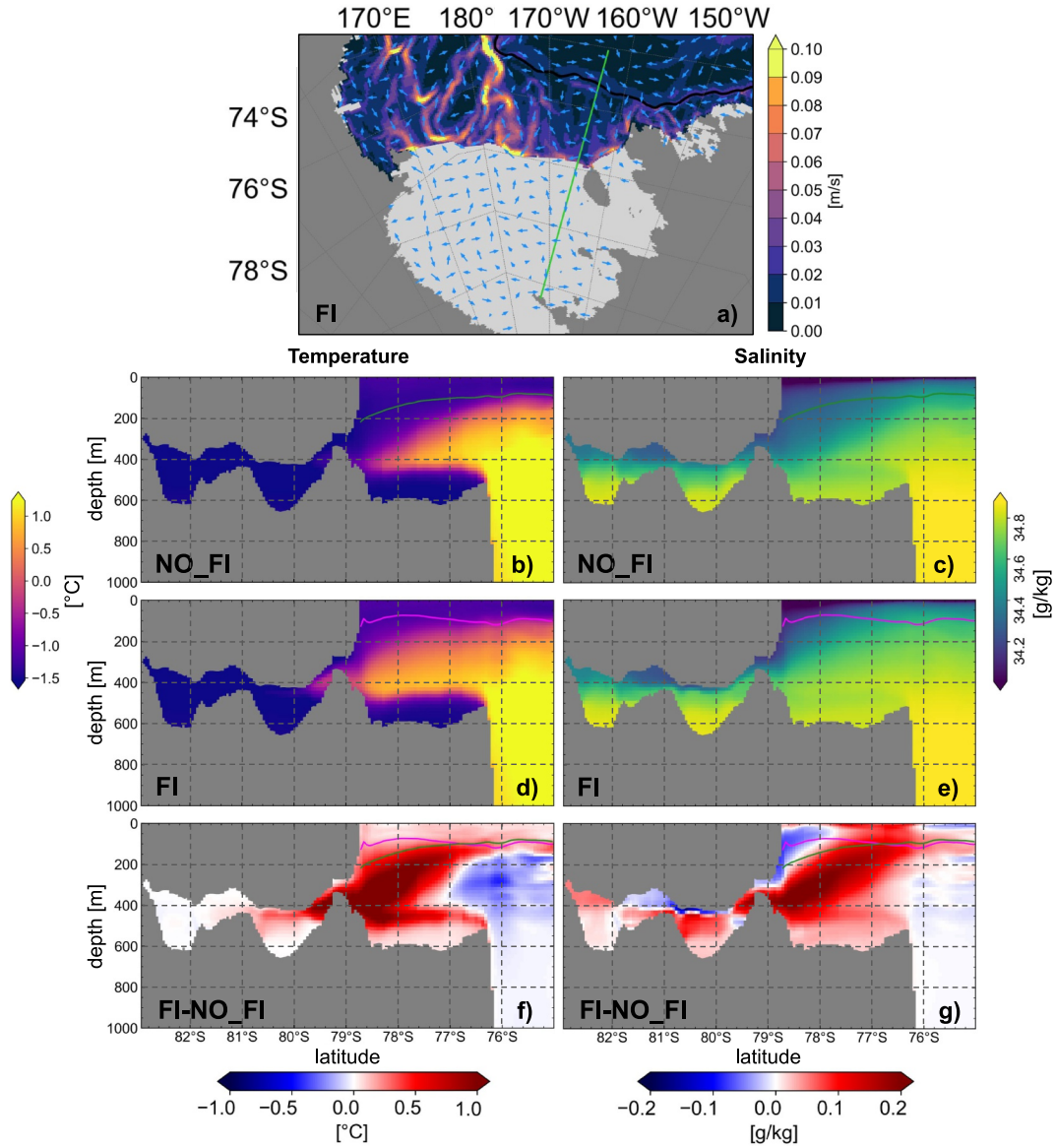



**Figure 14.** (a) Annual mean ocean current velocity and direction in the Ross Sea averaged over the 150–450 m depth range in the FI simulation for 2013–2017. The solid green line indicates the location of the section shown in panels (b–g), which extends from the surface to 1,000 m depth and across the Ross Sea and Ice Shelf cavity. Annual mean temperature along the section for the NO_FI simulation (b), the FI simulation (d), and their difference (FI-NO_FI; f). Annual mean salinity along the section for the NO_FI simulation (c), the FI simulation (e), and their difference (FI-NO_FI; g). The annual mean mixed layer depth along the section is overlaid in panels (b–g) for FI (solid pink line) and NO_FI (solid green line). All panels show annual means over the period 2013–2017.

Houtz and Hayes Banks also influence regional water properties (Silvano et al., 2023). In the FI simulation, the presence of fast ice upstream of this sector and the small fast ice cover in front of the ice shelf (Figure 1) triggers a local shoaling of the mixed layer in front of the ice shelf, which enhances the intrusion of warm and saline waters onto the continental shelf and into the adjacent ice shelf cavities. To illustrate the mechanism, Figure 14 presents vertically averaged ocean velocities (150–450 m) together with cross-shelf sections of temperature and salinity. As a result of warmer water intrusion, basal melt increases, the melt water release intensifies, freshening the upper ocean along the ice shelf and toward the north (Figure 14g). This freshening further reduces the MLD (Figures 14f and 14g), reinforcing upper-ocean stratification. Finally, the shallower MLD (Figure 4e) facilitates a larger intrusion of warm (Figures 14b, 14d, and 14f) and saline (Figures 14c, 14e, and 14g) waters beneath the ice shelf. The associated increase in oceanic heat supply enhances basal ice shelf melt rates (e.g., Ross, Sulzberger,



21699291, 2026, 10, Downloaded from https://agupubs.onlinelibrary.wiley.com/doi/10.1029/2025JC023673 by Universite Catholique De Louvain, Wiley Online Library on [06/10/2026]. See the Terms and Conditions (https://onlinelibrary.wiley.com/terms-and-conditions) on Wiley Online Library for rules of use; OA articles are governed by the applicable Creative Commons License

21699291, 2026, 10, Downloaded from https://agupubs.onlinelibrary.wiley.com/doi/10.1029/2025JC023673 by Universite Catholique De Louvain, Wiley Online Library on [06/10/2026]. See the Terms and Conditions (https://onlinelibrary.wiley.com/terms-and-conditions) on Wiley Online Library for rules of use; OA articles are governed by the applicable Creative Commons License

Nickerson; Figure 11). Overall, the representation of fast ice promotes ISW formation (Figure 13c) in FI. In addition, the enhanced intrusion of saline waters onto the shelf contributes to the increase in bottom water density in FI (Figures 12e and 13c). The representation of fast ice is also responsible for a clear volumetric shift toward lower density water masses, evident in the leftward shift of the light arch of the T-S diagram (Figure 13c). This arch is also present in the upstream ASS. Meanwhile, the dense cone in the T-S diagram, corresponding to the densest water masses, emerges prominently in the CDS, EAS, and WSS. This dual presence in the RSS implies that this sector experiences two changes: a decrease in density of the AASW and an increase in density of HSSW when the fast ice scheme is activated. Nonetheless, it should be noted that, in this sector, fast ice has a limited impact on the dynamics of coastal polynyas and thereby on associated local water mass transformations.

In the ASS (150°W to 90°W), the bottom water density decreases on average by 0.028 kg $m^{-3}$ in FI compared to NO_FI. Beneath fast ice tongues (e.g., over Bear Ridge, near 110°W, 74°S, east of the Amundsen Polynya), the bottom water salinity increases (Figure 6e), yet bottom water density decreases (Figure 12e) in FI. The large increase in bottom water temperature in FI (Figure 5e) thus dominates the impact on bottom water density changes. Figure 13d corroborates this, showing an increase in the volume of lower density water masses in FI. The Amundsen Sea is characterized by warmer shelf waters compared to other Antarctic sectors (Figure 5c). Ice shelves such as Pine Island and Thwaites are known for their high basal melt rates, largely driven by warm water intrusions onto the continental shelf (Jenkins et al., 2018; Naughten et al., 2023; Thoma et al., 2008). In the FI simulation, fast ice noticeably affects the MLDs (Figure 4e) and induces a significant subsurface warming near ice shelf fronts (Figure 5e), leading to enhanced basal melting (Figure 11). These findings confirm the results of Bett et al. (2020), showing that it is worth including fast ice in future estimates of ice shelf melt rates in this sector, as done—in a simple way—in the projections of Jourdain et al. (2022), Naughten et al. (2023), and Mathiot and Jourdain (2023).

Finally, in the WSS (60°W to 30°W), the bottom water density increases by 0.019 kg $m^{-3}$ in FI compared to NO_FI on average (Figure 12e). This region is characterized by the formation of ISW beneath the Filchner-Ronne Ice Shelf, which is exported via the Filchner Trough and also by HSSW production near the western shelf break (Gordon & Ice Station Weddell Group of Principal Investigators and Chief Scientists, 1993; Hellmer et al., 2008; Huhn et al., 2008). However, melting at the base of the Filchner-Ronne Ice Shelf remains largely unchanged in the presence of fast ice in the model (Figure 11), suggesting that ISW modifications (Figure 13e) are not the main driver of the density increase. Instead, the densification appears to be a direct consequence of increased bottom water salinity (Figure 6e). Then, the more saline water is exported toward the shelf break via the Hughes Trough in FI. Overall, fast ice fosters the formation of denser shelf waters in the WSS (Figure 13e).

## 4. Discussion and Conclusion

In this study, we applied a recently developed method to represent Antarctic fast ice in an ocean-sea ice model. The method consists of restoring sea ice velocity toward zero where and when fast ice is observed. Using this approach, we explored the effects of the velocity-restoring fast ice scheme on Antarctic shelf water properties and ice shelf melt simulated by a 1/4° circum-Antarctic configuration of the NEMO-SI$^3$ ocean-sea ice model in hindcast experiments covering the period 2001–2017.

We found that the representation of Antarctic fast ice has a significant impact on the simulated ocean hydrography, particularly by redistributing sea ice production, with large consequences on the ocean surface mixed layer. Fast ice directly exerts a strong local control on the upper-ocean stratification: during the ice growing season, reduced brine rejection beneath the fast ice maintains fresher surface conditions and limits ocean vertical mixing. This change in vertical mixing leads to a surface cooling and a subsurface warming. This warming could be enhanced where and when the NO_FI simulation includes an active coastal polynya, although the mechanism leading to temperature differences does not depend on the presence of such a polynya. In summer, the insulating effect of fast ice reduces solar heating of near-surface waters, inducing cooling signals that can propagate at depth later in the season. Indirectly, fast ice enhances sea ice formation in coastal polynyas and at fast ice margins, strengthening brine rejection and promoting dense water formation in these key regions. However, we also showed that extensive fast ice tongues upstream of coastal polynyas, with their relatively low ice production, can reduce salinity in the polynyas themselves via advection of fresher surface waters, thereby counteracting the enhanced brine rejection effect.

21699291, 2026, 10, Downloaded from https://agupubs.onlinelibrary.wiley.com/doi/10.1029/2025JC023673 by Universite Catholique De Louvain, Wiley Online Library on [06/10/2026]. See the Terms and Conditions (https://onlinelibrary.wiley.com/terms-and-conditions) on Wiley Online Library for rules of use; OA articles are governed by the applicable Creative Commons License

The rate of ice shelf melt is significantly enhanced (+15.8%) by the subsurface warming, particularly where the mixed layer previously reached the seabed near ice shelf in the control simulation without fast ice. At the Antarctic scale, this highlights the importance of including fast ice in future assessments of ice shelf melt rates (see Figure 11 and Table S1 in Supporting Information S1). While this conclusion has previously been suggested regionally (e.g., Jourdain et al., 2022; Mathiot & Jourdain, 2023; Naughten et al., 2023; Van Achter, Fichefet, Goosse, & Moreno-Chamarro, 2022), our study demonstrates its broader relevance.

Both direct and indirect effects of Antarctic fast ice play an important role in controlling the DSW formation. While the mechanisms vary by sector, the presence of fast ice systematically modulates the formation and transformation of the shelf water masses. In regions such as Cape Darnley, Weddell Sea, and Ross Sea, fast ice enhances dense water formation via increased brine rejection and ice shelf melting. In contrast, sectors like the Amundsen Sea and Wilkes-Adélie exhibit bottom water density reductions, primarily driven by subsurface warming and surface freshening beneath the fast ice.

A key limitation of using sea ice velocity restoring toward zero to represent fast ice is its reliance on observational data, which are only available on the Antarctic circumpolar scale for the past two decades, restricting its applicability for long-term climate simulations. As expected, given the longer renewal timescales of off-shelf bottom waters relative to the simulation length, the impact of fast ice on bottom water salinity and temperature beyond the continental shelf (seafloor depths >1,500 m) appears negligible; however, differences may appear in longer (100–1,000 years) simulations. Furthermore, this method lacks a physical basis to capture processes such as thick fast ice formation through ridging or the influence of grounded icebergs on fast ice and on ocean circulation. A previous idealized study by Kusahara et al. (2010) shows the potential influence of grounded icebergs on ocean currents beneath fast ice. Consequently, the surface freshening advected from upstream fast ice tongues into coastal polynyas observed in our study is likely biased, as the model neglects the influence of icebergs on ocean circulation, although the extent of this bias remains uncertain. The warmer subsurface conditions associated with fast ice lead to enhanced ice shelf basal melting, which may in turn dampen the formation of DSW through the release of a large amount of freshwater. Therefore, our estimates of the impact of fast ice on DSW formation should be considered conservative. Importantly, incorporating fast ice may require model retuning to adapt ice shelf melt rates and avoid biases in future simulations. One possible avenue for improvement would be to reduce the salt and heat exchange coefficients used at the ocean-ice shelf interface. Since the response of basal melt rates to fast ice representation is heterogeneous in sign and particularly in magnitude, the potential adaptations may require regionally targeted parameter adjustments, rather than uniform modifications applied across all ice shelves.

Together, these limitations and the demonstrated role of Antarctic fast ice in coastal oceanic processes motivate a physically-based representation of sea ice-iceberg interactions in Antarctic-focused ESM studies. Recent advances in simulating iceberg grounding and ungrounding (Kostov et al., 2025; Olivé Abelló et al., 2025), combined with formulations of iceberg-sea ice interactions (Hunke & Comeau, 2011; Liu et al., 2022) and the inclusion of sea ice tensile strength (König Beatty & Holland, 2010), offer promising pathways toward systematic, process-based representation of Antarctic fast ice in ESM.

## Conflict of Interest

The authors declare no conflicts of interest relevant to this study.

## Availability Statement

The code of NEMO-SI$^3$ used is available from https://forge.nemo-ocean.eu/nemo/nemo/-/tree/4.2.2?ref_type=tags. Mixed layer depths, bottom shelf water densities, salinities, and temperatures, ice shelf basal melts, 3D fields of temperature and salinity averaged over 2013–2017 for the two simulations (FI and NO_FI) are available from https://doi.org/10.5281/zenodo.17473512. Sea ice concentration, sea ice thickness, sea ice production (in open-water and bottom growth), polynya frequency and polynya detection algorithm of Pirlet et al. (2025) are available from https://doi.org/10.5281/zenodo.17476130.

**Acknowledgments**
The authors thank the two anonymous reviewers for their valuable comments and suggestions, which significantly helped improve the manuscript. This research was conducted within the Belgian National Fund of Scientific Research (FNRS) project LICEPOD (PDR Grant T.0079.22) Computational resources have been provided by the supercomputing facilities of the UCLouvain (CISM/UCLouvain) and the Consortium des Equipements de Calcul Intensif en Fédération Wallonie Bruxelles (CECI), funded by the Fonds de la Recherche Scientifique—FNRS (F.R.S.-FNRS) (convention no. 2.5020.11) and by the Walloon Region. Open access publication funding provided by COUPERIN CY26.

## References

Adusumilli, S., Fricker, H. A., Medley, B., Padman, L., & Siegfried, M. R. (2020). Interannual variations in meltwater input to the Southern Ocean from Antarctic ice shelves. *Nature Geoscience*, *13*(9), 616–620. https://doi.org/10.1038/s41561-020-0616-z

Akhoudas, C. H., Sallée, J.-B., Haumann, F. A., Meredith, M. P., Garabato, A. N., Reverdin, G., et al. (2021). Ventilation of the abyss in the Atlantic sector of the Southern Ocean. *Scientific Reports*, *11*(1), 6760. https://doi.org/10.1038/s41598-021-86043-2

Barnier, B., Madec, G., Molines, J.-M., Treguier, A.-M., Le Sommer, J., Beckmann, A., et al. (2006). Impact of partial steps and momentum advection schemes in a global ocean circulation model at eddy-permitting resolution. *Ocean Dynamics*, *56*(5–6), 543–567. https://doi.org/10.1007/s10236-006-0082-1

Behrens, E., Rickard, G., Morgenstern, O., Martin, T., Osprey, A., & Joshi, M. (2016). Southern Ocean deep convection in global climate models: A driver for variability of subpolar gyres and Drake Passage transport on decadal timescales. *Journal of Geophysical Research: Oceans*, *121*(6), 3905–3925. https://doi.org/10.1002/2015JC011286

Bett, D. T., Holland, P. R., Naveira Garabato, A. C., Jenkins, A., Dutrieux, P., Kimura, S., & Fleming, A. (2020). The impact of the Amundsen Sea freshwater balance on ocean melting of the West Antarctic Ice Sheet. *Journal of Geophysical Research: Oceans*, *125*(9), e2020JC016305. https://doi.org/10.1029/2020JC016305

Bitz, C. M., Holland, M. M., Weaver, A. J., & Eby, M. (2001). Simulating the ice-thickness distribution in a coupled climate model. *Journal of Geophysical Research*, *106*(C2), 2441–2463. https://doi.org/10.1029/1999JC000113

Boucher, O., Servonnat, J., Albright, A. L., Aumont, O., Balkanski, Y., Bastrikov, V., et al. (2020). Presentation and evaluation of the IPSL-CM6A-LR climate model. *Journal of Advances in Modeling Earth Systems*, *12*(7), e2019MS002010. https://doi.org/10.1029/2019MS002010

Brook, E. J., & Buizert, C. (2018). Antarctic and global climate history viewed from ice cores. *Nature*, *558*(7709), 200–208. https://doi.org/10.1038/s41586-018-0172-5

Cougnon, E. A., Galton-Fenzi, B. K., Meijers, A. J. S., & Legrésy, B. (2013). Modeling interannual dense shelf water export in the region of the Mertz Glacier Tongue (1992–2007): Modeling Interannual Dense Shelf Water. *Journal of Geophysical Research: Oceans*, *118*(10), 5858–5872. https://doi.org/10.1002/2013JC008790

Davison, B. J., Hogg, A. E., Gourmelen, N., Jakob, L., Wuite, J., Nagler, T., et al. (2023). Annual mass budget of Antarctic ice shelves from 1997 to 2021. *Science Advances*, *9*(41), eadi0186. https://doi.org/10.1126/sciadv.adi0186

De Boyer Montégut, C., Madec, G., Fischer, A. S., Lazar, A., & Iudicone, D. (2004). Mixed layer depth over the global ocean: An examination of profile data and a profile-based climatology. *Journal of Geophysical Research*, *109*(C12), 2004JC002378. https://doi.org/10.1029/2004JC002378

de Lavergne, C., Vic, C., Madec, G., Roquet, F., Waterhouse, A. F., Whalen, C. B., et al. (2020). A parameterization of local and remote tidal mixing. *Journal of Advances in Modeling Earth Systems*, *12*(5), e2020MS002065. https://doi.org/10.1029/2020MS002065

Depoorter, M. A., Bamber, J. L., Griggs, J. A., Lenaerts, J. T. M., Ligtenberg, S. R. M., Van Den Broeke, M. R., & Moholdt, G. (2013). Calving fluxes and basal melt rates of Antarctic ice shelves. *Nature*, *502*(7469), 89–92. https://doi.org/10.1038/nature12567

Dupont, F., Dumont, D., Lemieux, J.-F., Dumas-Lefebvre, E., & Caya, A. (2022). A probabilistic seabed–ice keel interaction model. *The Cryosphere*, *16*(5), 1963–1977. https://doi.org/10.5194/tc-16-1963-2022

Engedahl, H. (1995). Use of the flow relaxation scheme in a three-dimensional baroclinic ocean model with realistic topography. *Tellus*, *47*(3), 365–382. https://doi.org/10.3402/tellusa.v47i3.11523

Flather, R. A. (1994). A storm surge prediction model for the northern Bay of Bengal with application to the cyclone disaster in April 1991. *Journal of Physical Oceanography*, *24*(1), 172–190. https://doi.org/10.1175/1520-0485(1994)024⟨0172:ASSPMF⟩2.0.CO;2

Fraser, A. D., Massom, R. A., Handcock, M. S., Reid, P., Ohshima, K. I., Raphael, M. N., et al. (2021). 18 year record of circum-Antarctic landfast sea ice distribution allows detailed baseline characterisation, reveals trends and variability. *Sea ice/Antarctic*. https://doi.org/10.5194/tc-2021-121

Fraser, A. D., Massom, R. A., Michael, K. J., Galton-Fenzi, B. K., & Lieser, J. L. (2012). East Antarctic Landfast Sea ice distribution and variability, 2000–08. *Journal of Climate*, *25*(4), 1137–1156. https://doi.org/10.1175/JCLI-D-10-05032.1

Fraser, A. D., Massom, R. A., Ohshima, K. I., Willmes, S., Kappes, P. J., Cartwright, J., & Porter-Smith, R. (2020). High-resolution mapping of circum-Antarctic landfast sea ice distribution, 2000–2018. *Earth System Science Data*, *12*(4), 2987–2999. https://doi.org/10.5194/essd-12-2987-2020

Fraser, A. D., Wongpan, P., Langhorne, P. J., Klekociuk, A. R., Kusahara, K., Lannuzel, D., et al. (2023). Antarctic Landfast Sea ice: A review of its physics, biogeochemistry and ecology. *Reviews of Geophysics*, *61*(2), e2022RG000770. https://doi.org/10.1029/2022RG000770

Gent, P. R., & Mcwilliams, J. C. (1990). Isopycnal mixing in ocean circulation models. *Journal of Physical Oceanography*, *20*(1), 150–155. https://doi.org/10.1175/1520-0485(1990)020⟨0150:IMIOCM⟩2.0.CO;2

Gill, A. (1973). Circulation and bottom water production in the Weddell Sea. *Deep-Sea Research and Oceanographic Abstracts*, *20*(2), 111–140. https://doi.org/10.1016/0011-7471(73)90048-X

Golledge, N. R., Keller, E. D., Gossart, A., Malyarenko, A., Bahamondes-Dominguez, A., Krapp, M., et al. (2025). Antarctic coastal polynyas in the global climate system. *Nature Reviews Earth & Environment*, *6*(2), 126–139. https://doi.org/10.1038/s43017-024-00634-x

Gorbunov, Y. A., Dyment, L. N., Losev, S. M., & Frolov, S. V. (2008). Medium-range forecasts of large ice cover discontinuities for hydrometeorological support of navigation in the Arctic basin. *Russian Meteorology and Hydrology*, *33*(9), 594–599. https://doi.org/10.3103/S1068373908090070

Gordon, A. L., & Ice Station Weddell Group of Principal Investigators and Chief Scientists. (1993). Weddell Sea exploration from ice station. *EOS Transactions of the American Geophysical Union*, *74*(11), 121–126. https://doi.org/10.1029/93EO00260

Gordon, A. L., Visbeck, M., & Huber, B. (2001). Export of Weddell Sea deep and bottom water. *Journal of Geophysical Research*, *106*(C5), 9005–9017. https://doi.org/10.1029/2000JC000281

Goutorbe, B., Poort, J., Lucazeau, F., & Raillard, S. (2011). Global heat flow trends resolved from multiple geological and geophysical proxies. *Geophysical Journal International*, *187*(3), 1405–1419. https://doi.org/10.1111/j.1365-246X.2011.05228.x

Griffies, S. M., Biastoch, A., Böning, C., Bryan, F., Danabasoglu, G., Chassignet, E. P., et al. (2009). Coordinated ocean-ice reference experiments (COREs). *Ocean Modelling*, *26*(1–2), 1–46. https://doi.org/10.1016/j.ocemod.2008.08.007

Gwyther, D. E., Kusahara, K., Asay-Davis, X. S., Dinniman, M. S., & Galton-Fenzi, B. K. (2020). Vertical processes and resolution impact ice shelf basal melting: A multi-model study. *Ocean Modelling*, *147*, 101569. https://doi.org/10.1016/j.ocemod.2020.101569

Hasumi, H. (2006). CCSR ocean component model (COCO) version 4.0. Retrieved from https://cir.nii.ac.jp/crid/1370004230122203264

Hellmer, H., Schröder, M., Haas, C., Dieckmann, G., & Spindler, M. (2008). The ISPOL drift experiment. *Deep Sea Research Part II: Topical Studies in Oceanography*, *55*(8–9), 913–917. https://doi.org/10.1016/j.dsr2.2008.01.001



21699291, 2026, 10, Downloaded from https://agupubs.onlinelibrary.wiley.com/doi/10.1029/2025JC023673 by Universite Catholique De Louvain, Wiley Online Library on [06/10/2026]. See the Terms and Conditions (https://onlinelibrary.wiley.com/terms-and-conditions) on Wiley Online Library for rules of use; OA articles are governed by the applicable Creative Commons License

Herraiz-Borreguero, L., Church, J. A., Allison, I., Peña-Molino, B., Coleman, R., Tomczak, M., & Craven, M. (2016). Basal melt, seasonal water mass transformation, ocean current variability, and deep convection processes along the Amery Ice Shelf calving front, East Antarctica. *Journal of Geophysical Research: Oceans*, *121*(7), 4946–4965. https://doi.org/10.1002/2016JC011858

Herraiz-Borreguero, L., Coleman, R., Allison, I., Rintoul, S. R., Craven, M., & Williams, G. D. (2015). Circulation of modified Circumpolar Deep Water and basal melt beneath the Amery Ice Shelf, East Antarctica. *Journal of Geophysical Research: Oceans*, *120*(4), 3098–3112. https://doi.org/10.1002/2015JC010697

Hersbach, H., Bell, B., Berrisford, P., Hirahara, S., Horányi, A., Muñoz-Sabater, J., et al. (2020). The ERA5 global reanalysis. *Quarterly Journal of the Royal Meteorological Society*, *146*(730), 1999–2049. https://doi.org/10.1002/qj.3803

Heuzé, C. (2021). Antarctic bottom water and north Atlantic deep water in CMIP6 models. *Ocean Science*, *17*(1), 59–90. https://doi.org/10.5194/os-17-59-2021

Heuzé, C., Heywood, K. J., Stevens, D. P., & Ridley, J. K. (2013). Southern Ocean bottom water characteristics in CMIP5 models. *Geophysical Research Letters*, *40*(7), 1409–1414. https://doi.org/10.1002/grl.50287

Huhn, O., Hellmer, H. H., Rhein, M., Rodehacke, C., Roether, W., Schodlok, M. P., & Schröder, M. (2008). Evidence of deep- and bottom-water formation in the western Weddell Sea. *Deep Sea Research Part II: Topical Studies in Oceanography*, *55*(8–9), 1098–1116. https://doi.org/10.1016/j.dsr2.2007.12.015

Hunke, E. C., & Comeau, D. (2011). Sea ice and iceberg dynamic interaction. *Journal of Geophysical Research*, *116*(C5), C05008. https://doi.org/10.1029/2010JC006588

Huot, P.-V., Kittel, C., Fichefet, T., Jourdain, N. C., & Fettweis, X. (2022). Effects of ocean mesoscale eddies on atmosphere–sea ice–ocean interactions off Adélie Land, East Antarctica. *Climate Dynamics*, *59*(1–2), 41–60. https://doi.org/10.1007/s00382-021-06115-x

Huot, P.-V., Kittel, C., Fichefet, T., Jourdain, N. C., Sterlin, J., & Fettweis, X. (2021). Effects of the atmospheric forcing resolution on simulated sea ice and polynyas off Adélie Land, East Antarctica. *Ocean Modelling*, *168*, 101901. https://doi.org/10.1016/j.ocemod.2021.101901

Intergovernmental Panel on Climate Change. (2022). *The ocean and cryosphere in a changing climate: Special report of the intergovernmental panel on climate change*. Cambridge University Press.

Jackett, D. R., & Mcdougall, T. J. (1997). A neutral density variable for the world's oceans.

Jacobs, S. S., Amos, A. F., & Bruchhausen, P. M. (1970). Ross sea oceanography and Antarctic bottom water formation. *Deep-Sea Research and Oceanographic Abstracts*, *17*(6), 935–962. https://doi.org/10.1016/0011-7471(70)90046-X

Jenkins, A. (1991). A one-dimensional model of ice shelf-ocean interaction. *Journal of Geophysical Research*, *96*(C11), 20671–20677. https://doi.org/10.1029/91JC01842

Jenkins, A., Shoosmith, D., Dutrieux, P., Jacobs, S., Kim, T. W., Lee, S. H., et al. (2018). West Antarctic Ice Sheet retreat in the Amundsen Sea driven by decadal oceanic variability. *Nature Geoscience*, *11*(10), 733–738. https://doi.org/10.1038/s41561-018-0207-4

Jourdain, N. C., Mathiot, P., Burgard, C., Caillet, J., & Kittel, C. (2022). Ice Shelf basal melt rates in the Amundsen Sea at the end of the 21st century. *Geophysical Research Letters*, *49*(22), e2022GL100629. https://doi.org/10.1029/2022GL100629

Kimmritz, M., Danilov, S., & Losch, M. (2016). The adaptive EVP method for solving the sea ice momentum equation. *Ocean Modelling*, *101*, 59–67. https://doi.org/10.1016/j.ocemod.2016.03.004

Kitade, Y., Shimada, K., Tamura, T., Williams, G. D., Aoki, S., Fukamachi, Y., et al. (2014). Antarctic bottom water production from the Vincennes Bay Polynya, East Antarctica. *Geophysical Research Letters*, *41*(10), 3528–3534. https://doi.org/10.1002/2014GL059971

König Beatty, C., & Holland, D. M. (2010). Modeling Landfast Sea ice by adding tensile strength. *Journal of Physical Oceanography*, *40*(1), 185–198. https://doi.org/10.1175/2009JPO4105.1

Kostov, Y., Holland, P. R., Hogan, K. A., Smith, J. A., Jourdain, N. C., Mathiot, P., et al. (2025). Modelled dynamics of floating and grounded icebergs, with application to the Amundsen Sea. https://doi.org/10.5194/egusphere-2025-2423

Kusahara, K., Hasumi, H., Fraser, A. D., Aoki, S., Shimada, K., Williams, G. D., et al. (2017). Modeling ocean–cryosphere interactions off Adélie and George V land, East Antarctica. *Journal of Climate*, *30*(1), 163–188. https://doi.org/10.1175/JCLI-D-15-0808.1

Kusahara, K., Hasumi, H., & Tamura, T. (2010). Modeling sea ice production and dense shelf water formation in coastal polynyas around East Antarctica. *Journal of Geophysical Research*, *115*(C10), 2010JC006133. https://doi.org/10.1029/2010JC006133

Large, W., & Yeager, S. (2004). *Diurnal to decadal global forcing for ocean and sea-ice models: The data sets and flux climatologies (Technical Report)*. UCAR/NCAR. https://doi.org/10.5065/D6KK98Q6

Lemieux, J. F., Dupont, F., Blain, P., Roy, F., Smith, G. C., & Flato, G. M. (2016). Improving the simulation of landfast ice by combining tensile strength and a parameterization for grounded ridges: Modeling LANDFAST ICE. *Journal of Geophysical Research: Oceans*, *121*(10), 7354–7368. https://doi.org/10.1002/2016JC012006

Lemieux, J. F., Lei, J., Dupont, F., Roy, F., Losch, M., Lique, C., & Laliberté, F. (2018). The impact of tides on simulated landfast ice in a Pan-Arctic ice-ocean model. *Journal of Geophysical Research: Oceans*, *123*(11), 7747–7762. https://doi.org/10.1029/2018JC014080

Lemieux, J. F., Tremblay, L. B., Dupont, F., Plante, M., Smith, G. C., & Dumont, D. (2015). A basal stress parameterization for modeling landfast ice. *Journal of Geophysical Research: Oceans*, *120*(4), 3157–3173. https://doi.org/10.1002/2014JC010678

Lipscomb, W. H. (2001). Remapping the thickness distribution in sea ice models. *Journal of Geophysical Research*, *106*(C7), 13989–14000. https://doi.org/10.1029/2000JC000518

Liu, Y., Losch, M., Hutter, N., & Mu, L. (2022). A new parameterization of coastal drag to simulate landfast ice in deep marginal Seas in the Arctic. *Journal of Geophysical Research: Oceans*, *127*(6), e2022JC018413. https://doi.org/10.1029/2022JC018413

Liu, Y., Losch, M., Tremblay, L. B., & Janout, M. (2025). Landfast ice in the Kara Sea stabilizes the Arctic halocline and may slow down Atlantification of the Eurasian Basin. *Communications Earth & Environment*, *6*(1), 423. https://doi.org/10.1038/s43247-025-02360-8

Liu, Y., Moore, J. C., Cheng, X., Gladstone, R. M., Bassis, J. N., Liu, H., et al. (2015). Ocean-driven thinning enhances iceberg calving and retreat of Antarctic ice shelves. *Proceedings of the National Academy of Sciences*, *112*(11), 3263–3268. https://doi.org/10.1073/pnas.1415137112

Locarnini, M., Mishonov, A., Baranova, O., Boyer, T., Zweng, M., Garcia, H., et al. (2018). World ocean atlas 2018, volume 1: Temperature (Report). Retrieved from https://archimer.ifremer.fr/doc/00651/76338/

Madec, G., Bell, M., Blaker, A., Bricaud, C., Bruciaferri, D., Castrillo, M., et al. (2023). NEMO Ocean engine reference manual. https://doi.org/10.5281/ZENODO.1464816

Mahoney, A. R., Eicken, H., Gaylord, A. G., & Gens, R. (2014). Landfast sea ice extent in the Chukchi and Beaufort Seas: The annual cycle and decadal variability. *Cold Regions Science and Technology*, *103*, 41–56. https://doi.org/10.1016/j.coldregions.2014.03.003

Mahoney, A. R., Eicken, H., Gaylord, A. G., & Shapiro, L. (2007). Alaska landfast sea ice: Links with bathymetry and atmospheric circulation. *Journal of Geophysical Research*, *112*(C2), 2006JC003559. https://doi.org/10.1029/2006JC003559

Marinov, I., Gnanadesikan, A., Sarmiento, J. L., Toggweiler, J. R., Follows, M., & Mignone, B. K. (2008). Impact of oceanic circulation on biological carbon storage in the ocean and atmospheric $pCO_2$. *Global Biogeochemical Cycles*, *22*(3), 2007GB002958. https://doi.org/10.1029/2007GB002958



21699291, 2026, 10, Downloaded from https://agupubs.onlinelibrary.wiley.com/doi/10.1029/2025JC023673 by Universite Catholique De Louvain, Wiley Online Library on [06/10/2026]. See the Terms and Conditions (https://onlinelibrary.wiley.com/terms-and-conditions) on Wiley Online Library for rules of use; OA articles are governed by the applicable Creative Commons License

Martin, A., Houssais, M.-N., Le Goff, H., Marec, C., & Dausse, D. (2017). Circulation and water mass transports on the East Antarctic shelf in the Mertz Glacier region. *Deep Sea Research Part I: Oceanographic Research Papers*, *126*, 1–20. https://doi.org/10.1016/j.dsr.2017.05.007

Massom, R. A., Harris, P., Michael, K. J., & Potter, M. (1998). The distribution and formative processes of latent-heat polynyas in East Antarctica. *Annals of Glaciology*, *27*, 420–426. https://doi.org/10.3189/1998AoG27-1-420-426

Mathiot, P., Barnier, B., Gallée, H., Molines, J. M., Sommer, J. L., Juza, M., & Penduff, T. (2010). Introducing katabatic winds in global ERA40 fields to simulate their impacts on the Southern Ocean and sea-ice. *Ocean Modelling*, *35*(3), 146–160. https://doi.org/10.1016/j.ocemod.2010.07.001

Mathiot, P., Jenkins, A., Harris, C., & Madec, G. (2017). Explicit representation and parametrised impacts of under ice shelf seas in the *z* coordinate ocean model NEMO 3.6. *Geoscientific Model Development*, *10*(7), 2849–2874. https://doi.org/10.5194/gmd-10-2849-2017

Mathiot, P., & Jourdain, N. C. (2023). Southern Ocean warming and Antarctic ice shelf melting in conditions plausible by late 23rd century in a high-end scenario. *Ocean Science*, *19*(6), 1595–1615. https://doi.org/10.5194/os-19-1595-2023

Meredith, M. P., & Brandon, M. A. (2017). Oceanography and sea ice in the Southern Ocean. In D. N. Thomas (Ed.), *Sea ice* (1st ed., pp. 216–238). Wiley. https://doi.org/10.1002/9781118778371.ch8

Miller, U. K., Zappa, C. J., Gordon, A. L., Yoon, S.-T., Stevens, C., & Lee, W. S. (2024). High Salinity Shelf Water production rates in Terra Nova Bay, Ross Sea from high-resolution salinity observations. *Nature Communications*, *15*(1), 373. https://doi.org/10.1038/s41467-023-43880-1

Morales Maqueda, M. A., Willmott, A. J., & Biggs, N. R. T. (2004). Polynya dynamics: A review of observations and modeling. *Reviews of Geophysics*, *42*(1), 2002RG000116. https://doi.org/10.1029/2002RG000116

Nakata, K., Ohshima, K. I., & Nihashi, S. (2021). Mapping of active frazil for Antarctic coastal polynyas, with an estimation of sea-ice production. *Geophysical Research Letters*, *48*(6), e2020GL091353. https://doi.org/10.1029/2020GL091353

Nakayama, Y., Timmermann, R., Rodehacke, C. B., Schröder, M., & Hellmer, H. H. (2014). Modeling the spreading of glacial meltwater from the Amundsen and Bellingshausen Seas. *Geophysical Research Letters*, *41*(22), 7942–7949. https://doi.org/10.1002/2014GL061600

Naughten, K. A., Holland, P. R., & De Rydt, J. (2023). Unavoidable future increase in West Antarctic ice-shelf melting over the twenty-first century. *Nature Climate Change*, *13*(11), 1222–1228. https://doi.org/10.1038/s41558-023-01818-x

Nihashi, S., & Ohshima, K. I. (2015). Circumpolar mapping of Antarctic coastal polynyas and Landfast Sea Ice: Relationship and variability. *Journal of Climate*, *28*(9), 3650–3670. https://doi.org/10.1175/JCLI-D-14-00369.1

Ohshima, K. I., Fukamachi, Y., Williams, G. D., Nihashi, S., Roquet, F., Kitade, Y., et al. (2013). Antarctic Bottom Water production by intense sea-ice formation in the Cape Darnley polynya. *Nature Geoscience*, *6*(3), 235–240. https://doi.org/10.1038/ngeo1738

Olivé Abelló, A., Mathiot, P., Jourdain, N. C., Kostov, Y., Holland, P. R., Gascoin, S., & Rousset, C. (2025). Iceberg grounding enhances the release of freshwater on the Antarctic Continental Shelf. *Journal of Geophysical Research: Oceans*, *130*(10), e2025JC022857. https://doi.org/10.1029/2025JC022857

Orsi, A. H., Johnson, G., & Bullister, J. (1999). Circulation, mixing, and production of Antarctic Bottom Water. *Progress in Oceanography*, *43*(1), 55–109. https://doi.org/10.1016/S0079-6611(99)00004-X

Orsi, A. H., & Wiederwohl, C. L. (2009). A recount of Ross Sea waters. *Deep Sea Research Part II: Topical Studies in Oceanography*, *56*(13–14), 778–795. https://doi.org/10.1016/j.dsr2.2008.10.033

Paolo, F. S., Gardner, A. S., Greene, C. A., Nilsson, J., Schodlok, M. P., Schlegel, N.-J., & Fricker, H. A. (2023). Widespread slowdown in thinning rates of West Antarctic ice shelves. *The Cryosphere*, *17*(8), 3409–3433. https://doi.org/10.5194/tc-17-3409-2023

Patara, L., & Böning, C. W. (2014). Abyssal ocean warming around Antarctica strengthens the Atlantic overturning circulation. *Geophysical Research Letters*, *41*(11), 3972–3978. https://doi.org/10.1002/2014GL059923

Pirlet, N., Fichefet, T., Vancoppenolle, M., Fraser, A. D., Mathiot, P., Rousset, C., et al. (2025). Benefits of a landfast ice representation on simulated Antarctic Sea ice and coastal Polynya dynamics. *Journal of Geophysical Research: Oceans*, *130*(9), e2024JC022032. https://doi.org/10.1029/2024JC022032

Portela, E., Rintoul, S. R., Herraiz-Borreguero, L., Roquet, F., Bestley, S., Van Wijk, E., et al. (2022). Controls on dense shelf water formation in four East Antarctic Polynyas. *Journal of Geophysical Research: Oceans*, *127*(12), e2022JC018804. https://doi.org/10.1029/2022JC018804

Prather, M. J. (1986). Numerical advection by conservation of second-order moments. *Journal of Geophysical Research*, *91*(D6), 6671–6681. https://doi.org/10.1029/JD091iD06p06671

Purkey, S. G., & Johnson, G. C. (2010). Warming of global abyssal and deep Southern Ocean waters between the 1990s and 2000s: Contributions to global heat and Sea level rise budgets. *Journal of Climate*, *23*(23), 6336–6351. https://doi.org/10.1175/2010JCLI3682.1

Rignot, E., Jacobs, S., Mouginot, J., & Scheuchl, B. (2013). Ice-shelf melting around Antarctica. *Science*, *341*(6143), 266–270. https://doi.org/10.1126/science.1235798

Rintoul, S. R., & Bullister, J. L. (1999). A late winter hydrographic section from Tasmania to Antarctica. *Deep Sea Research Part I: Oceanographic Research Papers*, *46*(8), 1417–1454. https://doi.org/10.1016/S0967-0637(99)00013-8

Roberts, M. J., Reed, K. A., Bao, Q., Barsugli, J. J., Camargo, S. J., Caron, L.-P., et al. (2025). High-Resolution Model Intercomparison Project phase 2 (HighResMIP2) towards CMIP7. *Geoscientific Model Development*, *18*(4), 1307–1332. https://doi.org/10.5194/gmd-18-1307-2025

Roquet, F., Madec, G., McDougall, T. J., & Barker, P. M. (2015). Accurate polynomial expressions for the density and specific volume of seawater using the TEOS-10 standard. *Ocean Modelling*, *90*, 29–43. https://doi.org/10.1016/j.ocemod.2015.04.002

Rousset, C., Vancoppenolle, M., Madec, G., Fichefet, T., Flavoni, S., Barthélemy, A., et al. (2015). The Louvain-La-Neuve sea ice model LIM3.6: Global and regional capabilities. *Geoscientific Model Development*, *8*(10), 2991–3005. https://doi.org/10.5194/gmd-8-2991-2015

Sallée, J.-B., Pellichero, V., Akhoudas, C., Pauthenet, E., Vignes, L., Schmidtko, S., et al. (2021). Summertime increases in upper-ocean stratification and mixed-layer depth. *Nature*, *591*(7851), 592–598. https://doi.org/10.1038/s41586-021-03303-x

Sarmiento, J. L., & Toggweiler, J. R. (1984). A new model for the role of the oceans in determining atmospheric $pCO_2$. *Nature*, *308*(5960), 621–624. https://doi.org/10.1038/308621a0

Shchepetkin, A. F., & McWilliams, J. C. (2005). The regional oceanic modeling system (ROMS): A split-explicit, free-surface, topography-following-coordinate oceanic model. *Ocean Modelling*, *9*(4), 347–404. https://doi.org/10.1016/j.ocemod.2004.08.002

Sigman, D. M., Hain, M. P., & Haug, G. H. (2010). The polar ocean and glacial cycles in atmospheric $CO_2$ concentration. *Nature*, *466*(7302), 47–55. https://doi.org/10.1038/nature09149

Silvano, A., Purkey, S., Gordon, A. L., Castagno, P., Stewart, A. L., Rintoul, S. R., et al. (2023). Observing Antarctic bottom water in the Southern Ocean. *Frontiers in Marine Science*, *10*, 1221701. https://doi.org/10.3389/fmars.2023.1221701

Sterlin, J., Orval, T., Lemieux, J.-F., Rousset, C., Fichefet, T., Massonnet, F., & Raulier, J. (2024). Influence of the representation of landfast ice on the simulation of the Arctic sea ice and Arctic Ocean halocline. *Ocean Dynamics*. https://doi.org/10.1007/s10236-024-01611-0

Storkey, D., Blaker, A. T., Mathiot, P., Megann, A., Aksenov, Y., Blockley, E. W., et al. (2018). UK Global Ocean GO6 and GO7: A traceable hierarchy of model resolutions. *Geoscientific Model Development*, *11*(8), 3187–3213. https://doi.org/10.5194/gmd-11-3187-2018



21699291, 2026, 10, Downloaded from https://agupubs.onlinelibrary.wiley.com/doi/10.1029/2025JC023673 by Universite Catholique De Louvain, Wiley Online Library on [06/10/2026]. See the Terms and Conditions (https://onlinelibrary.wiley.com/terms-and-conditions) on Wiley Online Library for rules of use; OA articles are governed by the applicable Creative Commons License

Swart, N. C., Martin, T., Beadling, R., Chen, J.-J., Danek, C., England, M. H., et al. (2023). The Southern Ocean Freshwater Input from Antarctica (SOFIA) Initiative: Scientific objectives and experimental design. *Geoscientific Model Development*, *16*(24), 7289–7309. https://doi.org/10.5194/gmd-16-7289-2023

Tamura, T., Ohshima, K. I., & Nihashi, S. (2008). Mapping of sea ice production for Antarctic coastal polynyas. *Geophysical Research Letters*, *35*(7), 2007GL032903. https://doi.org/10.1029/2007GL032903

Thoma, M., Jenkins, A., Holland, D., & Jacobs, S. (2008). Modelling Circumpolar Deep Water intrusions on the Amundsen Sea continental shelf, Antarctica. *Geophysical Research Letters*, *35*(18). https://doi.org/10.1029/2008gl034939

Van Achter, G., Fichefet, T., Goosse, H., & Moreno-Chamarro, E. (2022). Influence of fast ice on future ice shelf melting in the Totten Glacier area, East Antarctica. *The Cryosphere*, *16*(11), 4745–4761. https://doi.org/10.5194/tc-16-4745-2022

Van Achter, G., Fichefet, T., Goosse, H., Pelletier, C., Sterlin, J., Huot, P.-V., et al. (2022). Modelling landfast sea ice and its influence on ocean–ice interactions in the area of the Totten Glacier, East Antarctica. *Ocean Modelling*, *169*, 101920. https://doi.org/10.1016/j.ocemod.2021.101920

Vancoppenolle, M., Fichefet, T., Goosse, H., Bouillon, S., Madec, G., & Maqueda, M. A. M. (2009). Simulating the mass balance and salinity of Arctic and Antarctic sea ice. 1. Model description and validation. *Ocean Modelling*, *27*(1–2), 33–53. https://doi.org/10.1016/j.ocemod.2008.10.005

Vancoppenolle, M., Jourdain, N. C., Fichefet, T., Fraser, A. D., Massonnet, F., Mathiot, P., et al. (2025). Why icebergs and their interactions with sea ice should be included in Earth System models? *Bulletin of the American Meteorological Society*. https://doi.org/10.1175/BAMS-D-25-0322.1

Vancoppenolle, M., Rousset, C., Blockley, E., Aksenov, Y., Feltham, D., Fichefet, T., et al. (2023). SI3, the NEMO sea ice engine. https://doi.org/10.5281/ZENODO.7534900

Williams, G., & Bindoff, N. (2003). Wintertime oceanography of the adélie depression. *Deep Sea Research Part II: Topical Studies in Oceanography*, *50*(8), 1373–1392. https://doi.org/10.1016/S0967-0645(03)00074-2

Williams, G. D., Bindoff, N. L., Marsland, S. J., & Rintoul, S. R. (2008). Formation and export of dense shelf water from the Adélie Depression, East Antarctica. *Journal of Geophysical Research*, *113*(C4), 2007JC004346. https://doi.org/10.1029/2007JC004346

Williams, G. D., Herraiz-Borreguero, L., Roquet, F., Tamura, T., Ohshima, K. I., Fukamachi, Y., et al. (2016). The suppression of Antarctic bottom water formation by melting ice shelves in Prydz Bay. *Nature Communications*, *7*(1), 12577. https://doi.org/10.1038/ncomms12577

World Meteorological Organization. (2014). Wmo sea-ice nomenclature: Terminology, codes and illustrated glossary (computer software manual no. WMO/OMM/BMO-No. 259). Retrieved from https://globalcryospherewatch.org/reference/wmo259.php(Edition1970-2014)

Zalesak, S. T. (2012). The design of flux-corrected transport (FCT) algorithms for structured grids. In D. Kuzmin, R. Löhner, & S. Turek (Eds.), *Flux-corrected transport: Principles, algorithms, and applications* (pp. 23–65). Springer Netherlands. https://doi.org/10.1007/978-94-007-4038-9_2

Zhou, S., Dutrieux, P., Giulivi, C., Silvano, A., Auckland, C., Abrahamsen, P., et al. (2025). Southern ocean moored time series (south of 60°S) (ocean ice d1.1) [Dataset]. https://doi.org/10.17882/99922

Zuo, H., Balmaseda, M. A., Tietsche, S., Mogensen, K., & Mayer, M. (2019). The ECMWF operational ensemble reanalysis–analysis system for ocean and sea ice: A description of the system and assessment. *Ocean Science*, *15*(3), 779–808. https://doi.org/10.5194/os-15-779-2019

Zweng, M., Reagan, J., Seidov, D., Boyer, T., Locarnini, M., Garcia, H., et al. (2019). World ocean atlas 2018, volume 2: Salinity. In *NOAA Atlas NESDIS 61 (report)*.



21699291, 2026, 10, Downloaded from https://agupubs.onlinelibrary.wiley.com/doi/10.1029/2025JC023673 by Universite Catholique De Louvain, Wiley Online Library on [06/10/2026]. See the Terms and Conditions (https://onlinelibrary.wiley.com/terms-and-conditions) on Wiley Online Library for rules of use; OA articles are governed by the applicable Creative Commons License